ISSN 1849–0751 (On–line)
ISSN 0013–7448 (Print)
UDK 621.31

https://doi.org/10.37798/EN2022712

Journal of Energy

VOLUME 71 Number 2 | 2022

ENERGIJA 71

Journal of Energy

Scientific Professional Journal Of Energy, Electricity, Power Systems
Online ISSN 1849–0751, Print ISSN 0013–7448, VOL 71
https://doi.org/10.37798/EN2022712

Published by
HEP d.d., Ulica grada Vukovara 37, HR–10000 Zagreb
HRO CIGRÉ, Berislavićeva 6, HR–10000 Zagreb

EDITORIAL

The first p aper " Development o f a B attery M anagement S ystem f or Centralized Control of a Battey Cluster" presents the development of a supervisory battery management system (BMS) that collects active power, reactive power, and state of charge measurements from installed battery storage units, enabling active and reactive power control. The BMS includes an HMI user interface that allows users to monitor and control the batteries, and the batteries communicate with the PLC via Modbus TCP/IP protocol. The PLC and HMI communicate via PROFINET. The BMS was designed for battery units applied in households and was installed in the Smart Grid Laboratory (SGLab) at the University of Zagreb Faculty of Electrical Engineering and Computing. The primary objectives of the BMS were to collect measurements from the batteries, display them on the HMI screen, and create active and reactive power management functions, as well as state of charge balancing functions.

The second paper "Mechanical and Ist Chemical Cleaning of NEK Steam Generators" discusses the sludge removal process carried out during outages on two steam generators (SGs) at the Krško Nuclear Power Plant (NEK). The SGs are a critical point where five major plant systems converge, and sludge removal takes place on the secondary side at the top of the tube sheet. The paper describes the traditional Sludge Lancing (SL) method, Inner Bundle Lancing (IBL) method, and Chemical Cleaning (CC) method used for the first time in 2019. Televisual inspections (TVI) are performed after sludge removal to assess hard sludge areas and search for foreign objects. Maintaining the highest level of U-tube integrity is crucial, as any leaks could potentially release radioactive material. The paper details the workflow of sludge removal activities during the 2019 outage and concludes that the combined chemical and mechanical cleaning process met the expectations in terms of sediment removed, cleanliness, and preventing future dent growth.

The third paper, "Determining the Transmission Capacity of Existing Transmission Lines Under High Wind Generation Conditions," addresses one of the key challenges in modern power systems with increasing renewable penetration. The authors analyze how high levels of wind generation influence the thermal and operational limits of existing transmission lines. By considering meteorological conditions, conductor characteristics, and real operating constraints, the paper demonstrates that transmission capacity can be significantly increased under favorable wind conditions through dynamic line rating approaches. The study provides valuable insights into how existing infrastructure can be utilized more efficiently without immediate investment in new lines. The results are particularly relevant for transmission system operators facing congestion issues and rapid growth of wind power, offering a practical framework for enhancing grid flexibility and supporting the secure integration of renewable energy sources.

The fourth paper, "MELCOR-to-MELCOR Coupling Method in Severe Accident Analysis Involving Core and Spent Fuel Pool," presents an advanced methodology for analyzing complex severe accident scenarios in nuclear power plants. The authors introduce a coupling approach that enables simultaneous and consistent simulation of accident progression in both the reactor core and the spent fuel pool using the MELCOR code. This method improves the representation of interactions between different plant areas during extreme events, providing a more comprehensive safety assessment. The paper highlights the importance of integrated modeling for understanding heat transfer, radionuclide release, and system responses under beyond-design-basis conditions. The proposed approach contributes to enhanced accident analysis capabilities and supports the development of more robust safety strategies in nuclear engineering and regulatory practice.

The fifth paper, "Power Variability of Wind and Solar Production Portfolio in the Republic of Croatia," investigates the temporal variability of renewable energy generation by analyzing combined wind and solar power production. Using real production data, the authors assess how the complementary nature of wind and solar resources affects overall power fluctuations. The study demonstrates that portfolio-based integration can reduce variability compared to single-source generation, thereby improving system predictability and operational planning. Special attention is given to seasonal and short-term variations relevant for power system balancing. The findings provide important guidance for system operators, planners, and policymakers in designing renewable portfolios that enhance reliability while supporting decarbonization goals. This work contributes to a deeper understanding of renewable integration challenges in national power systems.

Igor Kuzle
Editor–in–Chief

Journal of Energy

VOLUME 71 Number 2 | 2022

journal homepage: http://journalofenergy.com/

Development of a Battery Management System for Centralized Control of a Battery Cluster

Tamara Trogrlić, Mateo Beus

***Summary* — The purpose of this paper is to establish a supervisory battery management system which collects active power, reactive power and state of charge measurements from the installed battery storage units and enables active and reactive power control. In addition, an HMI user interface was designed to allow the user to monitor and control the batteries. The batteries communicate with the PLC via Modbus TCP/IP protocol. The communication enables the exchange of measured power and state of charge values between the PLC and batteries, as well as setting the desired power setpoint values and battery activation signals. The PLC and HMI communicate via PROFINET. The battery storage units are installed in Smart Grid Laboratory (SGLab) at the University of Zagreb Faculty of Electrical Engineering and Computing.**

***Keywords* — battery management system, Modbus TCP/IP, PLC, HMI, user interface.**

I. Introduction

At a time when the impact of electric power industry on the environment is gaining importance, new technologies are being developed to help the power system face the challenges of integrating renewable power sources into the system. An example of these new technologies which can help increase the flexibility of the existing power system are batteries, especially when used with photovoltaic (PV) systems. In that regard, the authors in [1] introduced the control strategy to achieve decentralized power management of a PV/battery hybrid unit in a droop-controlled islanded microgrid. Furthermore, the authors in [2] introduced a control strategy designed for hybrid energy storage system. In the proposed control strategy battery storage is used to compensate for slow charging power surges, while supercapacitors are applied to compensate for the fast charging surges. Additionally, in [3] the authors analyzed the configuration, design and operation of a grid with large PV penetration. In order to increase operational flexibility the proposed grid configuration also included a utility scale battery storage system connected to the grid through an independent inverter. In [4], a hybrid control strategy for PV and battery storage system in a stand-alone DC microgrid is proposed. Researchers in [5] developed a control strategy to achieve fully autonomous power management of multiple photovoltaic (PV)/battery hybrid units in islanded microgrids. The control strategy introduced in that paper had the ability to autonomously coordinate with dispatchable droop controlled units. By and large, batteries require a monitoring and control system to maximize their efficiency, but also to help re- searchers to better understand and improve existing technolo- gies. Interesting research in terms of the BMS development has been presented in [6]- [8]. In that regard the authors in [6] presented the BMS design for the application in the electric vehicles, while the authors in [7] introduced an advanced BMS for the application in smart grid infrastructure. In [8] the authors developed a hardware-in-the-loop (HIL) simulation battery model for purposes of BMS testing on a commercial HIL simulator. Additionally, in [9]- [10] the authors provided an extensive overview of the BMS designs for the application in the smart grid environment. Furthermore, the papers [11]- [12] deal with the advanced design of the BMS. In [11] the authors presented design and implementation of a BMS for the industrial internet of things (IIoT) enabled applications, while in [12] the authors presented the development of a BMS whose operation is based on the application of an Multi-Objective Gravitational Search Algorithm to schedule the best battery allocation.

Furthermore, the authors in [13] elaborated the concept of a virtual inertia provision using battery energy storage system.

This paper describes the development of a supervisory BMS (Battery Management System) application for battery units applied in households. The control algorithm is implemented using a PLC (Programmable Logic Controller), while the HMI's (Human-Machine-Interface) touch panel enables an intuitive user-friendly interface. The main goals of the designed BMS were to collect the chosen measurements from the batteries and display them on the HMI screen, and to create both active and reactive power management functions as well as SOC balancing functions. Establishing the communication between the batteries, PLC and HMI was of the utmost importance for the BMS to work. The paper is structured as follows. The established laboratory setup that is used for development of the BMS is described in the Section II. Section III provides a detailed overview of the developed BMS, from establishing communication to the designed functionalities. Experimental results are presented in the Section IV.

II. Laboratory Setup

This section gives an overview of VARTA Pulse 6 energy storage [15], SIMATIC ET200-SP PLC [18] and SIMATIC

TP1200 Comfort Panel HMI device [20]. Figure 1 illustrates the general overview of the equipment that is used to establish

(Corresponding author: Mateo Beus)

Tamara Trogrlić and Mateo Beus are with the University of Zagreb Faculty of Electrical Engineering and Computing,

Zagreb, Croatia (e-mail: tamara.trogrlic@fer.hr, mateo.beus@fer.hr)

Tamara Trogrlić, Mateo Beus, Development of a Battery Management System for Centralized Control of a Battery Cluster, Journal of Energy, vol. 71 Number 2 (2022), 3–9

https://doi.org/10.37798/2022712415

the necessary laboratory setup. As shown in Figure 1 the-communication network used to establish the laboratory setup is Ethernet-based and uses Modbus TCP and PROFINET industrial communication protocols.

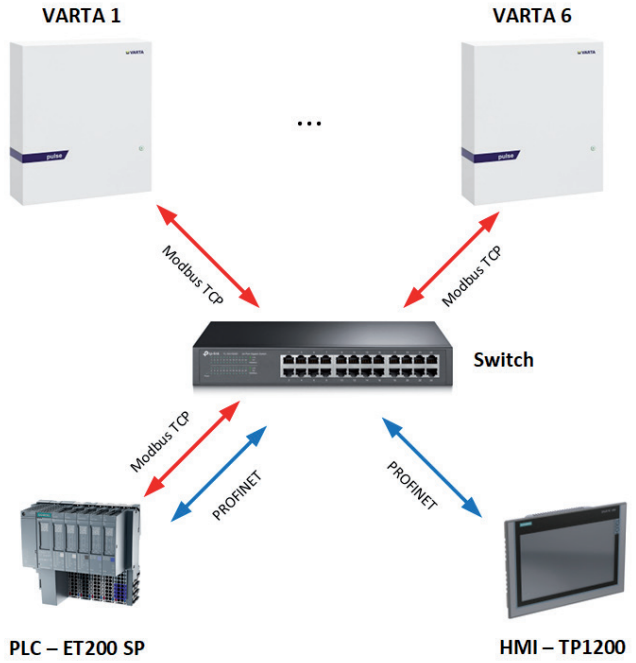

Fig. 1. General overview of the laboratory setup in SGLab

hand, if the PV energy production does not meet the object's needs, the electric current direction is from the grid into the object and the battery is discharged (if it has a sufficient SOC) with the goal to minimize the consumption of electrical energy from the grid. However, it is important to note that the above-mentioned sensor is disabled in the current laboratory setup so that the battery storage units can be controlled from an external system, such as a SCADA (Supervisory Control and Data Acquisition) system. Each battery storage unit is equipped with an Ethernet interface that was used to establish communication with the PLC via the Modbus TCP/IP protocol. Figure 2 shows the installed battery units in the lab.

Fig. 2. VARTA Pulse 6 battery units in SGLab

A. VARTA Pulse 6 energy storage

To explore the possibilities of energy storage systems and the-ir monitoring and management capabilities, six VARTA Pulse 6 battery storage units were installed in the Smart Grid Laboratory (SGLab) at the University of Zagreb Faculty of Electrical Engineering and Computing [14]. Since each battery unit has a single-phase inverter, a pair of two battery units is connected in each phase in order to establish a well balanced three-phase battery storage system.

The batteries' technical characteristics are displayed in Table I.

TABLE I

VARTA Pulse 6 technical characteristics [14]

Nominal capacity	6.5 kWh
Max. AC charge/discharge power	2.5/2.3 kW
Depth of discharge	90%
Electrochemistry	NMC
Mains connection	230V AC, 50 Hz, 1-phase
Mains configuration	TT-systems, TN-systems
Max. current output	11A
Protection class	IP33
Ambient conditions	+5°C to +30°C
Recommended circuit protection	B 16A MCB

First and foremost, the described battery storage system is designed for use in households with installed PV systems to get the most out of the locally produced energy [16]. With that in mind, an electric current sensor which controls the charging and discharging is included in the battery storage system's additional equipment. The sensor is installed just after the electricity meter and monitors the electric current direction: if the direction is from the object into the grid while the battery's state of charge (SOC) is less than the maximum SOC, the battery is charged. On the other

B. Programmable Logic Controller SIMATIC ET200-SP

SIMATIC ET200-SP station is a flexible, modular, and compact system from Siemens for various automation ap- plications. The station configuration can expand up to 64 modules, including digital and analog I/O modules [17]. I/O modules were not used for this application, since all necessary inputs and outputs are exchanged via Modbus TCP between the PLC and batteries. Using an interface module enables the communication with a central PLC if the station is used as distributed I/O [18]. The PLC has a CPU 1512SP-1 PN module with the functionalities of a Siemens S7-1500 series CPU [19]. The module has a 3-port PROFINET interface. Ports 1 and 2 require a bus adapter, while port 3 has an integrated RJ45 socket. The CPU module needs a 24V DC power supply and has a reverse polarity protection. A server module, which serves as an electrical and mechanical con- nection to the backplane bus and enables the monitoring of power supply voltage, is added to the CPU module. The CPU allows for up to 4000 defined blocks, which include Data Blocks (DB), Function Blocks (FB), Functions (FC), and Organizational Blocks (OB). The developed BMS algo- rithm uses two Organisational Blocks (OBs). The first OB1

- Main (contains Functions (FCs) which output final active and reactive power setpoints and activation signals) and OB30

- Communication (contains configured Modbus Clients and power monitoring functions). The block Main is executed with each PLC cycle, while Communication is a cyclic interrupt block which executes every 100 ms. Cyclic interrupt is used since the measured values don't change rapidly and such a delay in sending setpoint values to the batteries is insignificant. The FC's in Main use auxiliary FC's responsible for smaller tasks, such as a FC used for SOC regulation which checks the SOC of a battery and determines the corresponding power setpoint. Data Blocks (DBs) are

Tamara Trogrlić, Mateo Beus, Development of a Battery Management System for Centralized Control of a Battery Cluster, Journal of Energy, vol. 71 Number 2 (2022), 3–9
https://doi.org/10.37798/2022712415

used to organize measured and calculated data, as well as parameters needed for Modbus clients. The PLC supports following programming languages (IEC 61131-3): LAD (Ladder Diagram), FBD (Function Block Diagram), STL (Statement List), SCL (Structured Control Language) and GRAPH. LAD programming language was used for programming the BMS application in the PLC. The CPU supports various communications protocols, such as IP protocol, PROFINET IO, Open IE communication, OPC UA and Modbus TCP. It can have up to 128 simultaneously active connections, including those connected either via the CPU's integrated interfaces or via the communication processor mod- ule. Furthermore, the PLC can be connected to the Human – Machine Interface (HMI) via PROFINET to allow the user to easily control and monitor the battery storage units by means of a graphic user interface, which will be discussed later. The connection is created in the *Devices and networks* window of TIA Portal by connecting the Ethernet ports of the PLC and the HMI. The PLC and HMI are then in the same subnet. Their IP addresses must be set accordingly. In addition to having unique IP addresses, the devices communicating via PROFINET also need to have unique PROFINET device names.

C. SIMATIC TP1200 Comfort Panel

The chosen HMI device for this application is a SIMATIC TP1200 Comfort Panel from Siemens, which is designed as a touch screen. It has a TFT (thin-film-transistor) display, which is an LCD (liquid-crystal display) variant, with a 12.1-inch screen diagonal [20]. Control elements include only numeric and alphanumeric onscreen keyboards, but can be expanded with up to 40 direct keys (touch buttons). The required supply voltage is 24V DC, with a permissible range between 19.2V and 28.8 V. The panel has an x86 type processor, Flash and RAM memory, and 12 MB available memory for user data. It comes with a pre-installed Windows CE operating system. The panel is equipped with a 2-port industrial Ethernet interface, one RS-485 interface and two USB 2.0 interfaces. The supported protocols include PROFINET, PROFIBUS, EtherNet/IP, MPI, IRT and PROFINET IO. HMI can be configured from TIA Portal, using either a WinCC Comfort, WinCC Advanced or WinCC Professional software. There is a message system with 32 alarm classes and configurable acknowledgement groups. In addition, recipe management is a particularly interesting functionality for industrial automation. The HMI can be used for process monitoring and control in combination with PLCs from manufacturers other than Siemens, such as Allen Bradley and Mitsubishi. Laboratory setup used for testing is shown in Figure 3. It consists (from left to right) of a 24V DC industrial power supply, the PLC, a network switch, the HMI and a laptop. The power supply powers the PLC and HMI. The PLC, HMI, batteries and laptop are connected to the switch using Ethernet cables so that they are in the same LAN network. The HMI's main screen (with default values, before reading the battery measurements) is displayed in Figure 4. It shows the batteries as icons and displays the measured active, reactive and apparent power values, as well as the SOC for each battery. Total active, reactive and apparent power values can be seen at the bottom of the screen. A drop-down menu for choosing the screen for different control mode (active/reactive power control and SOC control) can be seen in the bottom right corner.

There are separate screens for active power/SOC regulation and reactive power regulation, but their working principle is the same. First and foremost, a management function variant must be selected on the screen. Once it is selected, the corresponding input fields and switches appear on the screen. The screen allows manipulating the inputs of the selected func- tion only. If the selected active power management function changes, all battery units are deselected to prevent them from accidentally following another management function's outputs. However, if the selected reactive power regulation function changes, all reactive power setpoints are just reset to zero, to avoid affecting the battery unit selection of active power management functions.

To finish connecting the HMI with the PLC, a connection has to be created in HMI's *Connections* tab in the TIA Portal. The connection parameters include the interface type and the devices' IP addresses. The created connection is later used to link the HMI tags with the corresponding PLC tags. Objects, such as I/O fields, buttons and text fields, are added to the screens using drag-and-drop and linked to HMI tags. Layers were used to reduce the number of screens. Screen objects that belong to the same function were arranged in the same layer and their visibility was set so that they are visible only when that function is selected. The HMI collects user-controlled inputs which get forwarded to the PLC. The PLC performs the programmed logic using these inputs and sends the necessary outputs to the HMI so the process can be monitored by the user.

D. Modbus TCP/IP communications protocol

Modbus is a communications protocol developed in 1979 by the Modicon company. It is widely used in industrial automation thanks to its simplicity and flexibility. Master/slave is main working principle of the Modbus RTU or client/server in case of Modbus TCP. Slave devices receive data from or send data to a master device only upon getting a request from a master device. Slave devices cannot volunteer data. Every device communicating via Modbus is required to have

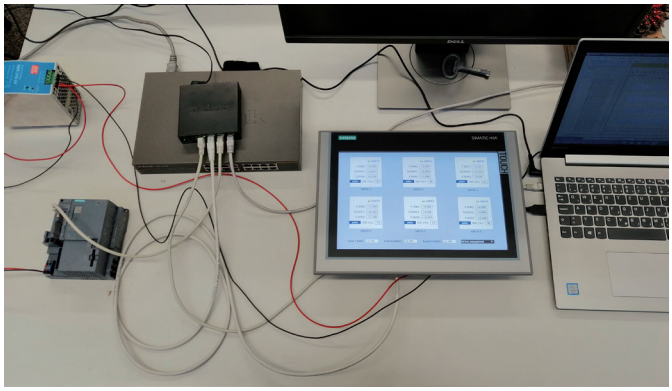

Fig. 3. Laboratory setup for BMS testing

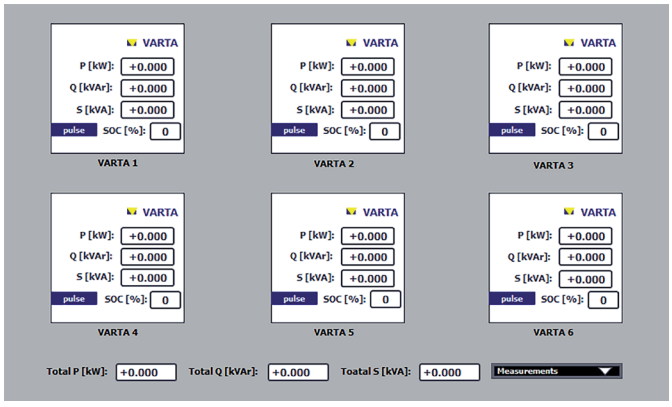

Figure 4. HMI main screen of developed BMS

a unique address. The most common variations of the Modbus protocol are Modbus RTU, Modbus ASCII, and Modbus TCP. Modbus RTU and Modbus ASCII are serial protocols which use a RS-232 or RS-485 interface, while Modbus TCP follows the OSI network model and can be used over the Ethernet infrastructure.

Another difference is that when using Modbus RTU and Modbus ASCII, there can be only one master device in the network, while Modbus TCP allows for multiple servers accessed by multiple clients. To use Modbus TCP, IP addresses of all devices in the network must be known. Modbus client device sends data to port 502 on server devices. Server device register types are listed in Table II [21].

TABLE II

MODBUS REGISTER TYPES

Memory block	Data type	*Client* access	*Server* access
Coils	Bool	read/write	read/write
Discrete inputs	Bool	read-only	read/write
Holding registers	Word	read/write	read/write
Input registers	Word	read-only	read/write

Address spaces for the above-mentioned memory blocks are: 00001-09999 for coils, 10001-19999 for discrete inputs, 20001-29999 for holding registers and 30001-39999 for input registers. The first digit of the address area determines the type of the register, and the remaining digits its location. Every Modbus command contains the address of a slave device that needs to be accessed, and a checksum to detect transmission errors. Modbus register table must be given for a device to know the addresses of its registers and what they stand for. In addition to the above, Modbus commands also contain Modbus function codes which define the desired action for the addressed register. Modbus functions can be regarded as either read or write functions and can moreover be differentiated by the type of the register being accessed. For example, the function code 3 stands for reading multiple holding registers. Exception codes are defined to help find the problem in case of a failed communication.

III. THE DEVELOPED BMS APPLICATION

A. ESTABLISHING COMMUNICATION OF THE PLC WITH THE BATTERIES

Successfully establishing the communication of the PLC with the batteries and the HMI is the first step to creating a battery management system. The PLC communicates with the battery storage units via Modbus TCP protocol over an Ethernet network. It enables retrieving the following mea- surements from the batteries: active power, apparent power, and state of charge. Furthermore, it enables sending the active and reactive power setpoints, along with an on/off signal, to the batteries. The absolute value of reactive power for each unit is calculated from the active and apparent power because the dedicated Modbus register for its measurement does not exist in the battery storage units. PLC acts as a Modbus client device, while the batteries have the role of a Modbus server. To establish a connection between the PLC and a battery storage unit, an already existing system function block in TIA Portal, called MB CLIENT, was used. One MB CLIENT represents one connection, and every connection needs a separate ID. Ev- ery battery needs separate connections for read and write func- tions because Modbus mode (MB MODE), which includes the Modbus function code, is an input to the MB CLIENT function block. Input parameters also include data address and data length, which together determine how many registers to read, starting at the given address, set according to the Modbus register table of the batteries. MB CLIENT needs a memory location for saving the acquired data or from which to send the data to the battery. Request and Disconnect parameters define if the communication requests are being sent and if the connection with the device is established, respectively. The last important input parameter is Connect, which contains the PLC's hardware-defined Ethernet interface ID, the connection ID, connection type, the requested device's IP address and the port number on the battery unit [22]. A separate data block was created for each connection, and it contains the described parameter configuration for the respective connection, along with an array in which the read data is stored or from which the data is written to the battery. An example of a data block with the above-mentioned parameters is given in Figure 5. That data block configures the connection for reading the data from the first battery. In total, 18 connections were created, 6 of which are used for reading the measurements, and the rest are used for writing power setpoints and on/off signals (since the reactive power setpoint register is not positioned

MB_Client_1R

	Name	Data type	Start ...	Comment
1	Static			
2	REQ	Bool	true	
3	DISCONNECT	Bool	false	
4	MB_MODE	USInt	103	Read multiple holding registers.
5	MB_DATA_ADDR	UDInt	1066	Start address.
6	MB_DATA_LEN	UInt	3	Number of registers.
7	Data_Varta1_R	Array[1..3] of Int		
8	Data_Varta1_R[1]	Int	0	Active power [W]
9	Data_Varta1_R[2]	Int	0	Apparent power [W]
10	Data_Varta1_R[3]	Int	0	SOC
11	STATUS	Word	16#0	
12	CONNECT	TCON_IP_v4		
13	InterfaceId	HW_ANY	64	HW-identifier of IE-interface submodule
14	ID	CONN_OUC	1	connection reference / identifier
15	ConnectionType	Byte	11	type of connection: 11=TCP/IP, 19=UDP (17
16	ActiveEstablished	Bool	true	active/passive connection establishment
17	RemoteAddress	IP_V4		remote IP address (IPv4)
18	ADDR	Array[1..4] of Byte		IPv4 address
19	ADDR[1]	Byte	192	IPv4 address
20	ADDR[2]	Byte	168	IPv4 address
21	ADDR[3]	Byte	66	IPv4 address
22	ADDR[4]	Byte	75	IPv4 address
23	RemotePort	UInt	502	remote UDP/TCP port number
24	LocalPort	UInt	0	local UDP/TCP port number

Fig. 5. MB CLIENT configuration parameters

immediately after target power and on/off signal registers, it cannot be simply written using the same MB CLIENT). Finally, all MB CLIENT blocks are gathered in a dedicated function in the cyclic interrupt block OB35, which is executed every 100 milliseconds.

B. BATTERY MANAGEMENT FUNCTIONS

The main purpose of this paper was to create the BMS and its corresponding HMI application. On the HMI's main screen, the battery storage units are represented as icons showing their respective active power, reactive power, apparent power, and state of charge measurements. The main screen also includes the batteries' combined active power, reactive power, and apparent power measurements.

1) Measurement acquisition and display: Measurements are acquired every time the OB35 cyclic interrupt block executes and are saved in their predefined memory locations. Since the power is measured in watts, but has to be displayed in kilowatts, an additional function was created to modify the acquired measurements. The function also calculates the batteries' reactive power, as seen in Equation 1, where Q_i is the i-th battery's reactive power in kilowatts while S_i and P_i are the i-th battery's apparent and active power in watts, respectively.

$$Q_i = \frac{\sqrt{S_i^2 - P_i^2}}{1000} \qquad i = 1, .., 6 \qquad (1)$$

Tamara Trogrlić, Mateo Beus, Development of a Battery Management System for Centralized Control of a Battery Cluster, Journal of Energy, vol. 71 Number 2 (2022), 3–9
https://doi.org/10.37798/2022712415

Reactive power sign is afterwards determined from the sign of the input percentage in reactive power regulation function. In addition, the same function is used to calculate the combined active power, reactive power, and apparent power values for display on the HMI's main screen. There is one HMI screen dedicated to the trend view of measured values and some setpoint values. It allows the user to select whether he wants to see active power, reactive power or SOC values by pressing the onscreen buttons. It also shows the user which management functions are selected, so the user knows which values to focus on.

2) Management functions: The BMS consists of three main management functions: active power regulation, which has two variants, SOC regulation with two variants and reactive power regulation, which also has two variants. Functions have their dedicated screens, where the user can select the management function variant and input the desired setpoints though the HMI's touch screen. Moreover, active and reactive power regulation should theoretically be able to operate indepen- dently, but it was found during laboratory testing that for reactive power regulation to work properly, the selected battery unit's active power setpoint must be different than zero (in other words, the batteries cannot have a solely reactive power output).

3) Active power regulation: Active power regulation has the following variants:

- Unit active power regulation: each battery unit's active power setpoint is set separately
- Group active power regulation: one active power setpoint is divided amongst the battery units

There is a dedicated function in the PLC which gathers all the necessary inputs for all variants, but only executes the code designed for the selected variant. The outputs of the function are final active power setpoints (integer value, in watts, as is required by the battery units) that are sent to the batteries via Modbus TCP, using the configured Modbus clients. The batteries have internal regulators which correct the setpoints if they are out of the allowed range.

Unit active power regulation allows the user to set a different charging (positive value) or discharging (negative value) power setpoint for each battery, as well as to turn the battery on or off. Active power setpoints are set through the HMI's input fields, while the on/off functionality is implemented as a switch. Input fields and switches (for all described functions) are connected to the HMI's corresponding tags, which are in turn connected to the PLC tags. These tags are inputs to the dedicated function in the PLC. That function takes care of making the necessary adjustments to the inputs, such as converting the data type and unit of measurement (kilowatts to watts). The HMI screen which enables the described unit active power regulation is shown in Figure 6.

Group active power regulation enables the user to input a sin- gle active power setpoint (either a positive or a negative value), which then gets equally divided amongst the six batteries. All battery units are activated or deactivated simultaneously using one switch on the HMI screen. The PLC function calculates the setpoint which gets sent to the batteries and once again makes the necessary adjustments.

4) SOC regulation: State of charge regulation is designed as follows:

- Unit SOC regulation: each battery unit's state of charge setpoint is set separately
- Group SOC regulation: all battery units get the same state of charge setpoint

SOC regulation is handled by the same function as active power regulation since it ultimately modifies active power

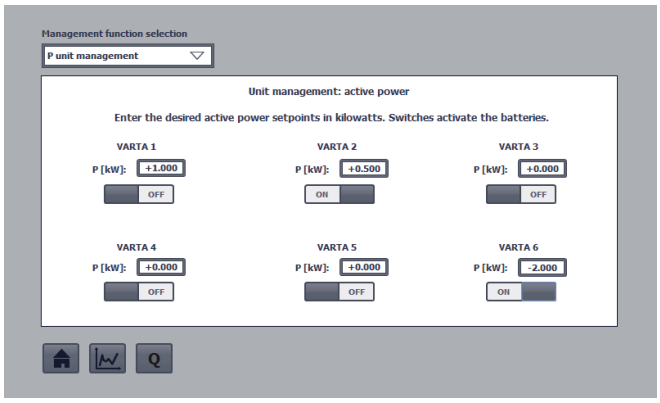

Fig. 6. Unit active power regulation HMI screen

setpoints.

Unit SOC regulation is focused on separately setting the desired state of charge setpoints (from 0% to 100%) for the batteries. The batteries are selected (but not activated or deactivated) via the already described switches. The algorithm is as follows: the function subtracts the selected battery's measured SOC from the SOC setpoint and takes the absolute value of the result. Active power setpoint magnitude is picked from four predefined values, shown in Table III, based on the calculated result (if the result is not zero). Greater SOC

TABLE III

CHARGING/DISCHARGING POWER VALUES DEPENDING ON THE SOC DIFFERENCE

/ΔSOC/ [%]	Charging/discharging power [W]
[50, 100]	2000
[30, 50)	1500
[10, 30)	1000
[0, 10)	500

difference results in a greater active power setpoint magnitude. If the measured SOC is greater than the SOC setpoint, the active power setpoint is sent to the function output as a negative value (discharging). If the measured SOC is lower than the SOC setpoint, the active power setpoint is sent to the function output as a positive value (charging). After the power setpoint is determined, the function output for battery activation is set accordingly. The outputs are sent to the battery units. This algorithm is repeated, adjusting the power setpoint as the battery charges or discharges, until the measured SOC matches the SOC setpoint or until the battery gets deselected. Then the power setpoint is 0, and the battery is deactivated. Group SOC regulation is very similar to Unit SOC regulation, the difference being that the same SOC setpoint is given for all batteries and all batteries are selected simultaneously. Determining the individual battery's active power setpoint and activation signal follows the same logic as described above.

5) Reactive power regulation: Reactive power regulation has the following variants:

- Unit reactive power regulation: each battery unit's reac- tive power setpoint is set separately
- Group reactive power regulation: one reactive power setpoint is divided amongst the battery units

As stated before, reactive power regulation requires the target

Tamara Trogrlić, Mateo Beus, Development of a Battery Management System for Centralized Control of a Battery Cluster, Journal of Energy, vol. 71 Number 2 (2022), 3–9
https://doi.org/10.37798/2022712415

battery storage unit to have an active power setpoint different than zero. There is a dedicated PLC function, which collects necessary inputs for both variants, but executes only the code needed for the selected variant. The function outputs are reactive power setpoints that are sent to the batteries via Modbus TCP.

Unit reactive power regulation enables the user to set a different reactive power setpoint for each battery. As opposed to the active power setpoints, reactive power setpoints must be set as a percentage of the rated power value, in a range [- 100%, 100%] for capacitive and inductive power, respectively. After ensuring that the input value is within limits, it gets forwarded to the output. Conversion of the set percentage into actual reactive power value is handled by the internal battery regulator and as such cannot be manipulated any further.

Group reactive power regulation allows the user to input a desired reactive power percentage setpoint, which then gets equally divided amongst the six battery units. The described functionality is shown by a flowchart in Figure 7. It must be noted that the sign of the input percentage is used to determine the sign of the reactive power value displayed on the main screen icons, since the batteries' displayed reactive power is not measured, but calculated from the apparent and active power values. Reactive power regulation is important because

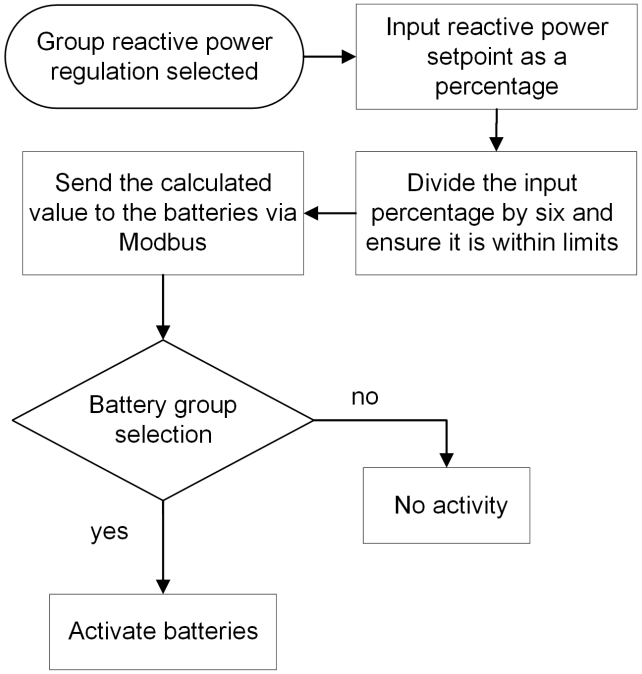

Fig. 7. Group SOC regulation flowchart

it enables voltage regulation using the battery units. Further insight into that functionality is beyond the scope of this paper.

6) Activating and deactivating the battery storage units: Since all management functions manipulate the activation and deactivation of batteries, an additional function was created to take all those influences into account. The function in- puts include the management function selection, HMI screen switches, and the on/off outputs of Unit SOC regulation and Group SOC regulation functions. The function contains a logic designed to determine whether a battery should be activated or not. The function's outputs are on/off signals for the batteries and are written to the batteries' respective registers via Modbus TCP.

IV. Experimental Results

The application was tested in SGLab using the described setup. The responses of the battery units to Group active power regulation and Group SOC regulation were recorded using TIA Portal's Trace functionality. Responses were plotted using Matlab. Figures 8 and 9 show the responses.

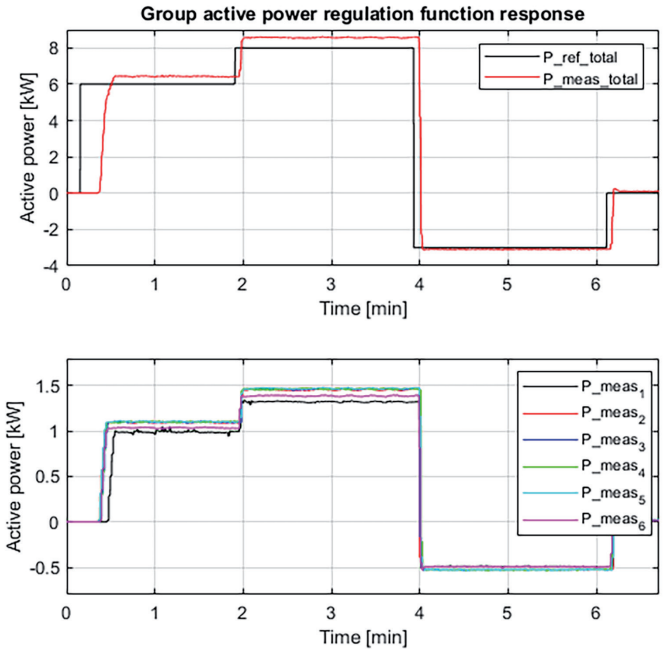

Fig. 8. Group active power regulation function response

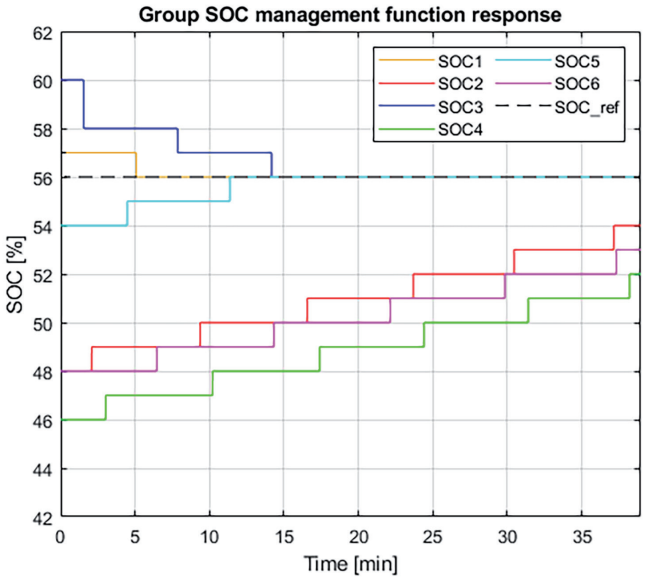

Fig. 9. Group SOC management function response

The first subplot in Figure 8 shows how the measured total active power follows the combined active power setpoint. The measured value varies slightly from the setpoint value because the internal controllers of the battery units can not precisely follow the setpoint value. The second subplot shows the distribution of the total measured active power amongst the batteries.

Figure 9 shows each battery's response to the Group SOC management function. The SOC setpoint is set to 56% for all batteries. Each battery initially had a different SOC value. It can be seen from the plot that the battery units 1, 3 and 5 reached

Tamara Trogrlić, Mateo Beus, Development of a Battery Management System for Centralized Control of a Battery Cluster, Journal of Energy, vol. 71 Number 2 (2022), 3–9
https://doi.org/10.37798/2022712415

the desired setpoint during the recorded interval, while the battery units 2, 4 and 6 are approaching the setpoint value.

V. Conclusion

This paper presents a battery management system developed for the six VARTA Pulse 6 battery storage units located in SGLab at the University of Zagreb Faculty of Electrical Engineering and Computing. The BMS was developed as a PLC application and enables monitoring and control of the installed batteries. Furthermore, an HMI user interface was created for the BMS. The user interface displays measurements obtained from the batteries and allows the control of the battery units through the HMI's touch panel. The introduced laboratory setup meets the set goals and can serve as a basis for the development of the voltage control algorithms or energy management systems that can be applied in low-voltage microgrids.

References

[1] H. Mahmood, D. Michaelson and J. Jiang, "Decentralized Power Man- agement of a PV/Battery Hybrid Unit in a Droop-Controlled Islanded Microgrid," *IEEE Trans. on Power Elec.*, vol. 30, no. 12, pp. 7215–7229, 2015.

[2] S.K. Kollimalla, M.K. Mishra and N.L. Narasamma, "Design and Analysis of Novel Control Strategy for Battery and Supercapacitor Storage System," *IEEE Trans. on Sust. Energy*, vol. 5, no. 4, pp. 1137– 1144, 2014.

[3] V. Rallabandi, O.M. Akeyo, N. Jewell and D.M. Ionel, "Incorporating Battery Energy Storage Systems Into Multi-MW Grid Connected PV Systems," *IEEE Trans. on Ind. App.*, vol. 55, no. 1, pp. 638–647, 2019.

[4] H.W. Yan et. al., "Minimizing Energy Storage Utilization in a Stand- Alone DC Microgrid Using Photovoltaic Flexible Power Control," *IEEE Trans. on Smart Grid*, vol. 12, no. 5, pp. 3755–3764, 2021.

[5] H. Mahmood and J. Jiang "Autonomous Coordination of Multiple PV/ Battery Hybrid Units in Islanded Microgrids," *IEEE Trans. on Smart Grid*, vol. 9, no. 6, pp. 6359–6368, 2016.

[6] K.W.E. Cheng, B.P. Divakar, H. Wu, K. Ding and H.F. Ho "Battery- Management System (BMS) and SOC Development for Electrical Vehi- cles," *IEEE Trans. on Vehicular Technology*, vol. 60, no. 1, pp. 76–88, 2011.

[7] A.T. Elsayed, C.R. Lashway and O.A. Mohammed "Advanced Battery Management and Diagnostic System for Smart Grid Infrastrucutre," *IEEE Trans. on Smart Grid*, vol. 7, no. 2, pp. 897–905, 2016.

[8] J.V. Barreras et al. "An advanced HIL Siumlation Battery Model for Battery Management System testing," *IEEE Trans. on Industry Appli- cations*, vol. 52, no. 6, pp. 5086–5099, 2016.

[9] H. Rahimi-Eichi, U. Ojha, F. Baronti and Mo-Yuen Chow "Battery Management System: An Overview of Its Application in the Smart Grid and Electric Vehicles," *IEEE Industrial Electronics Magazine*, vol. 7, no. 2, pp. 4–16, 2013.

[10] M.T. Lawder et al. "Battery Energy Storage System (BESS) and Battery Management System (BMS) for Grid-Scale Applications," *Proceedings of the IEEE*, vol. 102, no. 6, pp. 1014–1030, 2014.

[11] H.M.O. Canilang, A.C. Caliwag and W. Lim . "Design, Implementation, and Deployment of Modular Battery Management System for IIoT- Based Applications," *IEEE Access*, vol. 10, pp. 109008–109028, 2022.

[12] C.R. Sarin and G. Mani . "An Intelligent BMS With Probabilistic MOGSO Based CDMAS Integrating Edge Controller Analytics," *IEEE Access*, vol. 10, pp. 115802–115814, 2022.

[13] Matej Alandžak, Tomislav Plavsic, Dubravko Franković. Provision of Virtual Inertia Support Using Battery Energy Storage System, Journal of Energy – Energija, Vol. 70, No. 4, pp. 13–19, 2021

[14] "Smart Grid Laboratory (SGLab)," Faculty of Electrical Engineering and Computing, Department of Energy and Power Systems, University of Zagreb, [Online]. Available: https://sglab.fer.hr/. [Accessed: 24. 06. 2022].

[15] "Varta Pulse Datasheet," VARTA Storage GmbH, [Online]. Avail- able: https://solar-distribution.baywa-re.de/out/media/8-Pulse VARTA pulse datasheet en V08.pdf. [Accessed: 27. 05. 2022]"

[16] "Instruction Manual Varta Pulse,", VARTA Storage GmbH, [On- line]. Available: https://seasolargroup.com/wp-content/uploads/2018/08/ Instruction Manual VARTA pulse UK.pdf. Accessed: [27. 05. 2022].

[17] "SIMATIC ET 200SP – the compact IO system for the control cabinet," Siemens AG, [Online]. Available: https://new.siemens.com/global/ en/products/automation/systems/industrial/io-systems/et-200sp.html. Accessed: [20. 05. 2022].

[18] "SIMATIC ET 200SP Product Information," Siemens AG, [On- line]. Available: https://mall.industry.siemens.com/mall/en/WW/Catalog/ Products/10144488?tree=CatalogTree. Accessed: [20. 05. 2022].

[19] "CPU 1512SP-1 PN Product Information," Siemens AG, [Online]. Available: https://mall.industry.siemens.com/mall/en/WW/Catalog/Products/10239949?activeTab=productinformation&regionUrl=WW. Accessed: [22. 05. 2022].

[20] "SIMATIC HMI TP1200 Comfort Datasheet," Siemens AG, [Online]. Available: https://mall.industry.siemens.com/mall/en/it/Catalog/Product/6AV2124-0MC01-0AX0. Accessed: [09. 01. 2023].

[21] "Introduction to Modbus using LabVIEW," National Instruments, [Online]. Available: https://www.ni.com/en-rs/innovations/white-papers/12/ introduction-to-modbus-using-labview.html. Accessed: [21. 03. 2022].

[22] "Modbus/TCP with instructions 'MB CLIENT' and 'MB SERVER'," Siemens AG, [Online]. Available: https://support.industry.siemens.com/ cs/attachments/102020340/net modbus tcp s7-1500 s7-1200 en.pdf. Accessed: [21. 03. 2022]."

Journal of Energy

VOLUME 71 Number 2 | 2022

journal homepage: http://journalofenergy.com/

Mechanical and 1st Chemical Cleaning of NEK Steam Generators

Robert Kelavić, Marko Turalija

Summary — **Sludge removal is performed on two steam generators (SG's) at the Krško Nuclear Power Plant (NEK) during every outage. SG's are a meeting point of five major plant systems: Reactor Coolant System (RC) on the primary side and four systems on the secondary side – Auxiliary Feedwater System (AF), Blowdown System (BD), Main Feedwater System (FW), and Main Steam System (MS). Sludge removal activities take place on the secondary side of the SG's on the top of the tube sheet. It always consists of classical Sludge Lancing (SL) which is done by spraying water at different angles (30°, 90°, 150°) between the tube gaps in the steam generator tube bundle with a pressure of around 220 bars. Another method is Inner Bundle Lancing (IBL) which means spraying water directly inside the tube bundle with a traveling lance tape with a spraying nozzle at the end. Water is sprayed at an angle or directly on the top of the tube sheet with a robot-guided manipulator which is placed inside a steam generator. The manipulator and therefore the spraying action is controlled by an operator and at times it is fully autonomous to provide the highest protection measures possible. Another method of sludge removal which was for the first time utilized in 2019 at the Krško site was Chemical Cleaning (CC) of both SG's. During this process, a chemical was injected into the SG's through the BD system and periodically pumped between the two SG's to create a dynamic flow and maximize the cleaning effect. To achieve the best results, a constant temperature of the chemicals had to be maintained at all times. Upon completion of chemical cleaning, a rinsing phase was followed to remove any post-treatment chemicals. After all sludge removal activities, a televisual inspection (TVI) of the top of the tube sheet was performed to access the hard sludge area and to search for potential foreign objects in the SG's. If for instance an object of importance during TV inspection is found, an attempt to retrieve it would usually take place. Other methods of sludge removal such as upper bundle flushing or ultrasonic cleaning have not been implemented in NEK thus far. Since the power plant uprate in May 2000, NEK conducted SL on both SG's every outage also starting with IBL in 2013 and 2015, and the same method was used in the 2018 outage. During the outage in 2019, all three methods (SL, IBL, and CC) have been utilized with the main purpose to extend the full load operation of the plant, preventing and/or stopping denting processes in the SG's from occurring, reducing and stopping the build-up of hard sludge area to increase/sustain efficiency and remove foreign objects found in the SG's.SG's U-tubes are a barrier between the primary side coolant and the secondary side of NEK and the environment. Therefore, it is crucial to keep the highest level of integrity of the U-tubes because any leak could potentially mean a release of radioactive material into the atmosphere. This paper describes the purpose and workflow of sludge removal activities in the outage of 2019 in NEK.**

Keywords — **Steam Generators (SG's), Sludge Lancing (SL), Inner Bundle Lancing (IBL), Chemical Cleaning (CC), televisual inspection (TVI), Foreign Object Search and Retrieval (FOSAR), Krško Nuclear Power Plant (NEK)**

(Corresponding author: Robert Kelavić)
Robert Kelavić and Marko Turalija are with the Nuclear Power Plant Krško, Krško, Slovenia (e-mail: robert.kelavic@nek.si, marko.turalija@nek.si)

I. Introduction

NEK's steam generators are safety related components that are required to operate during normal, abnormal, and emergency conditions. During normal power operation, steam from steam generators is supplied to the turbine. During shutdown conditions, they are vital components in the decay heat removal process. Additionally, steam generators act as a third barrier for preventing radioactive releases into the environment. Due to this the cleanliness and operability of steam generators are vital for safe operation.

The driving factor to perform the Chemical Cleaning process at NEK was the discovery of the denting indications in 2018, which have also been confirmed later by re-evaluation of old Eddy Current Testing (ECT) data from 2006 and 2012. Denting is tube deformation due to material ingress into the space between the tube and tube sheet (for details see Chapter 2).

For SG #1 there was a significant increase in the hard sludge area between 2010 and 2016 which has been observed in the hot leg and is being constant until the last visual inspection in 2018- before CC. From the past data re-evaluation, there were 33 denting indications discovered in the hot leg, which were detected in 2006 and 2012. They are all located not only in the hard sludge area but also in its periphery. Since 2012 no new denting indications have been detected in the hot leg. The hard sludge area in the cold leg detected in 2012 and 2018 but were not detected in 2016, which is classified as an inconsistency. The 5 denting indications first time detected in the cold leg in 2018 are located in the hard sludge area and the low-flow zone. The low-flow zone was determined by Computational Fluid Dynamics (CFD) calculations.

For SG #2 there was a significant increase of hard sludge area between 2010 and 2016 in the hot leg, which has been constant until the last visual inspection in 2018 before Chemical Cleaning (CC) (similar to SG #1). In 2012 detected denting indications are located mainly outside of the hard sludge area seen in 2010. The newest detected indications in 2018 are located mainly in the periphery of

the hard sludge deposits. On the cold leg side of SG #2, no denting indications occurred.

In total at the end of the outage in 2018, NEK had confirmed 121 denting indications on both SG's collectively.

Mechanical sludge removal activities take place on the secondary side of the SG's on the top of the tube sheet. It consists of regular Sludge Lancing (SL) which is done by spraying water at different angles (30°, 90°, 150°) between the tube gaps in the steam generator tube bundle with a pressure of around 220 bars. Another method is Inner Bundle Lancing (IBL) which means spraying water directly inside the tube bundle directly on the top of the tube sheet with a robot-guided lance which is placed inside a steam generator. The robot is controlled by an operator and at times fully autonomous to provide the highest protection measures possible. After these activities, a televisual inspection (TVI) of the top of the tube sheet is performed to access the hard sludge area and to search for potential foreign objects in the SG's. If an object is found, an attempt to retrieve it would usually take place.

This paper describes the chemical cleaning process that took place during the outage in 2019 and the mechanical sludge removal process in NEK in the same period. Descriptions from setting up the equipment, differences between Sludge Lancing and Inner Bundle Lancing, additionally the purpose of TV inspection and FOSAR attempts will be included. The paper will offer an insight into the results of this year's outage as well.

II. Degradation Mechanism Denting

Denting is the mechanical deformation of the Steam generator tubes due to the external pressure forces acting on the outer diameter. When rapid growth of the material trapped in the crevices of tube-to-tube sheet occurs it causes a reduction in the tube diameter. Historically this degradation mechanism was mostly reported in crevices between tube-to-tube support plates, but recently the mechanism is seen as in NEK case in the tube-to-tube sheet locations despite the better tube material (690) than historically more susceptible alloy 600 and alloy 800.

There are two contributing factors for denting mechanism to occur. The first precondition is the existence of metallic iron in the crevice which can be present due to carbon steel tube sheet or due to the ingress of ferritic particles originating in the secondary water-steam cycle of the NPP.

A second contributing factor is the presence of oxygen in the area of said ferritic material. That leads to a rapid expansion of the volume of the impurities and thus affecting the outer/inner tube diameter. If the crevice is exposed to additional corrosive impurities the reaction is only accelerated by interacting with basic tube sheet material – often carbon steel. Since Top of Tube Sheet (TTS) hard sludge area is present in Krško SG's it blocks the free expansion of interacted materials thus causing them to deform SG's tubes.

The formation of the initial crevice in a tube-to-tube sheet is a consequence of the manufacturing process. Since it was not advisable to expand the tubes till the very top of the tube sheet due to the possibility of overexpansion and causing an initial crack, the hydraulic expansion was suspended 1~2 mm below TTS and therefore creating a small crevice in the described area.

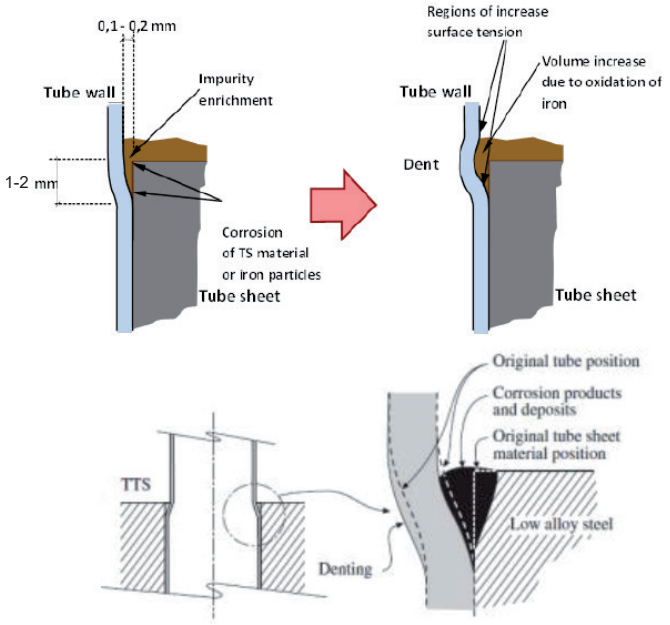

Fig. 1: Origination of dents on TTS

Regulation dictates that all tubes of SG must be checked with ECT every 5 years. ECT probes must fulfill something known as Fill Factor, which dictates that the probe diameter must be at least 80 % of the SG tube inner diameter. If the tube is inaccessible or its diameter is reduced due to excessive denting which causes that the fill factor criteria can't be met, the tube must be plugged preventatively. In the worst-case scenario denting can cause Outer Diameter Stress Corrosion Cracking (ODSCC).

2.1 Mitigation of denting

Denting can be mitigated with two main preventive actions and one corrective.

Firstly, the goal should be to limit particulate releases in the secondary water-steam cycle. This can be achieved by adhering to strict pH control or use of erosive/corrosive resistant materials, operating in steady state conditions, or injection of Film Forming Amines.

Secondly, the goal should be to limit oxygen levels in the secondary water-steam cycle. This can be achieved with strict control of Feed Water (FW) during On-Line (OL) operation, strict control of Auxiliary Feedwater (AF) during startup and shutdown, conservation of the secondary side of SGs with hydrazine, wet layup, and Film Forming Amines (FFA) during an outage.

Thirdly, the curative action is to remove the particulates accumulated on TTS. This can be achieved with the use of Blow Down (BD) system, Sludge Lancing (SL), Inner Bundle Lancing (IBL), chemical cleaning, Upper Bundle Flushing techniques, or installation of CY magnets. Newer options for sludge removal are the use of Poly Acrylic Acid (PAA) dispersants.

III. Chemical Cleaning – Flow of Events from the Decision to Execution

After the denting discovery in outage 2018, the technical debate was convened in NEK, where a mitigating strategy was presented and the decision for chemical cleaning in outage 2019 was formalized. Since NEK had no previous experience a benchmark of two NPPs that have performed where utilities used two different CC vendors. The first NPP was ASCO in Spain and the second was Belleville, France. This led to the realization of important

Robert Kelavić, Marko Turalija, Mechanical and 1st Chemical Cleaning of NEK Steam Generators, Journal of Energy, vol. 71 Number 2 (2022), 10–17
https://doi.org/10.37798/2022712413

factors the chemical cleaning process had to assure. The scale of equipment used for chemical cleaning had to be small enough to fit in the planned NEK area. Additionally, the process had to be efficient to clean the desired hard sludge area on TTS. Also, the process had to "fit" into the planned time schedule of the 2019 outage plan.

The bidding process was finished in March of 2019 and the selected vendor was Framatome GmbH for CC and mechanical cleaning operation. NEK had performed the QA audit the following month and received the "NEK Replacement Steam Generator Assessment Study" the month after. The study analysed a wide range of secondary chemistry data, the result of which was a selected process for chemical cleaning called DART LT - Deposit Accumulation Reduction Treatment at Low Temperatures with EDTA (95–100 °C). In June Adaptation study document followed which in detail defined the chemical cleaning procedure. Several performance tests were running simultaneously as well as presentations to the Slovenian regulatory body, Krško Safety Comitee (KSC), and internal organization. Additional walkdowns were performed and an equipment laydown area was prepared to facilitate the planned equipment.

IV. Setup of equipment

The arrival of equipment and its security check took place on 26/9/2019. The equipment was set up in the following days, which included the two separate units for SL and IBL processes both equipped with separate filtration systems and a Chemical injection container, two equipment containers, 2 additional quick shop containers, one large Waste sump trailer, and one insulated trailer for DD water, 4 TRAMETHYN – EDTA IBC double wall storage tanks, Severe Accident Mitigation Equipment (SAME) air compressor, and some additional spare equipment container.

The equipment was placed on the west side of the TB next to CY storage tanks.

Fig. 2: Equipment setup outside Reactor Building

Cable and hose routing was set up through Intermediate Building 100 (IB 100) elevation and consequently to Reactor Building (RB)100 and RB107 upon emergency hatch opening. Additionally, the heaters used for chemical cleaning and the distribution control were set up in IB100 as well to be as close as possible to SG's and to maximize the efficiency of the process.

After the arrival of personnel, a detailed pre-job briefing and basic general employee training were conducted. For of chemical/mechanical cleaning containment integrity is not required, so as soon that's the case, the equipment inside the RB and outside of it is connected and water was recirculated through both systems to ensure a leak-tight connection. During the first recirculation, a water sample is taken to prove the cleanliness of the cleaning equipment before the introduction of that water inside the NEK's SG's.

V. Operation

5.1 Chemical cleaning

The proposed sequence of sludge removal process was:

- SL1 on SG #2, Drying, TVI1 on SG #2 + FOSAR;
- CC on SG #1 and SG #2;
- Rinsing of SG #1 and SG #2 after CC;
- SL1 on SG #1, Drying, TVI1 on SG #1 + FOSAR, IBL on SG #1, SL2 on SG #1, Drying, TVI2 on SG #1 and FOSAR2;
- IBL on SG #2, SL2 on SG #2, Drying, TVI2 on SG #2 and FOSAR2.

The reason for the difference in the cleaning sequence was that SG #2 had reported foreign object (FO) in the non-desirable area during the 2018 outage and it was desirable to retrieve it first. Another reason was to maximize the efficiency of the chemical cleaning process, the RCS had to be drained as to prevent the heat reduction of the chemicals if it were to "escape" to the primary system through filled SG tubes.

5.2 Sludge Lancing (SL)

An SL robot is positioned and operated in the NO-Tube lane to remove the loosened sludge accumulated inside the hot leg (HL) and cold leg (CL) out of the tube bundle. The water is directed to the SG through high-pressure (HP) pumps (200 bar and 250 bar). Then the mixture of water plus sludge is removed from the SG by diaphragm pumps and trapped by high-performance filtering elements. The water is then conducted to a storage tank, to be re-injected into the steam generator by high pressure and peripheral jets pumps (see Figure 1). A bypass loop cools the water from the storage tank and purifies it so the SL cleaning process uses as neutral water as possible inside the SG's.

Because of the triangular pitch of the Krško SG's, the SL robot can be used in a 90° direction and 30°/150° from the NO-Tube lane. With the orientation of the jet stream in the direction of 30°, 90°, and 150°, it is possible to reach both a higher number of passes of the HP jets and various areas of the tube bundle compared to cleaning only at 90°. In this manner, the "shadow areas" which are behind the U-tubes from the perpendicular direction of the NO-Tube lane are also reached and cleaned.

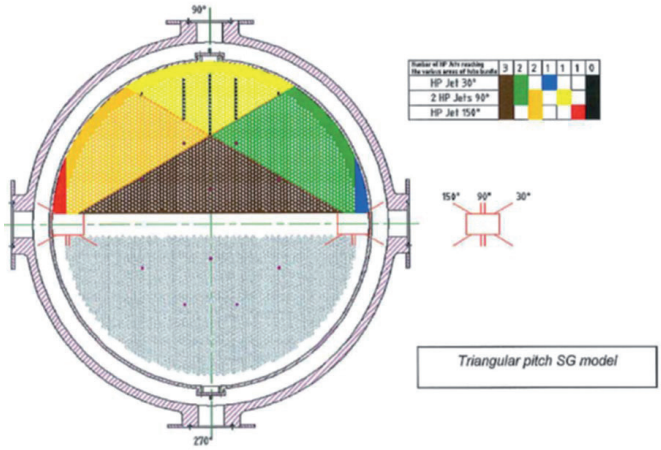

Fig. 3: Direction of High Pressure (HP) jets inside SG during the sludge lancing phase

Robert Kelavić, Marko Turalija, Mechanical and 1st Chemical Cleaning of NEK Steam Generators, Journal of Energy, vol. 71 Number 2 (2022), 10–17
https://doi.org/10.37798/2022712413

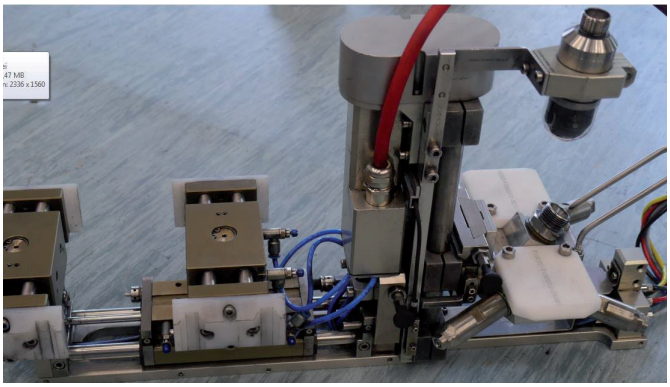

Fig. 4: SL manipulator

5.3 Inner Bundle Lancing (IBL)

A manipulator installed in the NO-Tube lane is equipped with an HP lance which can enter between tubes. Its goal is to break hard sludge deposits inside the tube bundle in the very low-velocity water area. The lance can be guided at a 90° angle and can reach the farthest area of SG tube rows. IBL lance travels between the tube bundle at different heights depending on the hard sludge situation. The spray head is spraying at a 60 ° angle which is constantly adjusted by the software program.

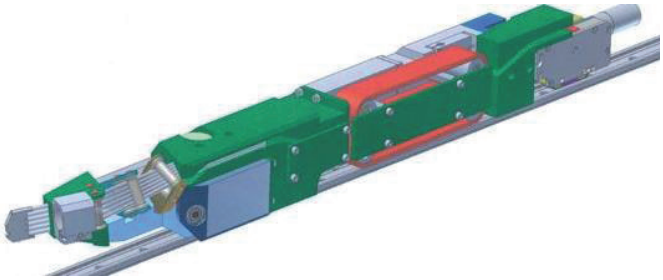

Figure 5: IBL manipulator

5.4 Drying

After SL, the SG must be prepared for TV inspection. Due to high humidity inside the SG after SL/IBL phase, the camera lens could get foggy and the image becomes blurry, therefore the drying equipment is introduced. The drying equipment consists of two intake units with HEPA filters, a double fan unit with a heater, and connection hoses. The discharge hoses are connected to the SG's inspection holes in the direction perpendicular to the NO-Tube lane. At least one secondary manway must be opened to effectively dry the SG before TV inspection. This process lasts about 10 hours.

5.5 TV inspection and FOSAR

Remote visual inspection is performed to inspect the inner tubes on the tube sheet, after the Sludge Lancing, to check the cleanliness, locate eventual foreign objects and check the result of the Sludge Lancing. A manipulator works the same as the IBL one, but instead of a high-pressure tape, the system uses a camera tape for inspection. Additionally, as a backup the vendor uses a crawler moving in the NO-Tube lane. The lance goes into each inter column at 90°, from the NO-Tube lane to the peripheral lane. The gap between each U-tube is approximately 3.6 mm when the tubes are new and no sludge has been accumulated. A small layer of sludge on the tube can block a camera path regardless of the fact, that the lens is only 2.7 mm thick. Another obstacle inside the SG is the space between a Tie-Rod and a U-tube.

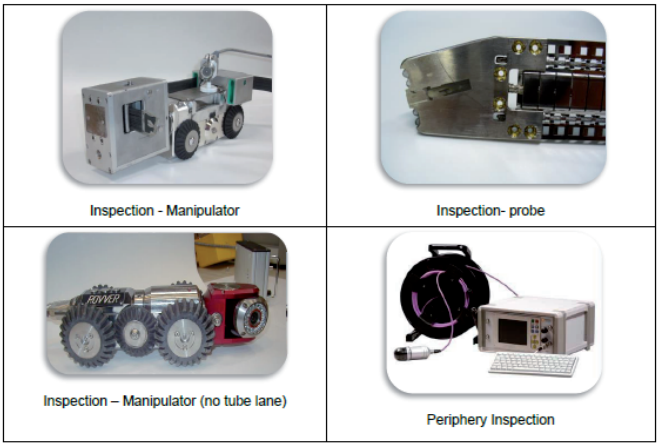

Fig. 6: TVI inspection tools

If a foreign object is found inside the SG, its location is carefully noted, the object is categorized, its length, weight and material is approximated. The categorization is carried out using the EPRI Technical Report 1020989 Steam Generator Management Program: Foreign Object Prioritization Strategy for Triangular Pitch Steam Generators. Based on the shape, size, and position of the object, its general location inside the SG, and some other factors, a decision will be made if a retrieval attempt is performed. TV crawler in that case acts as a guide for the operator who manually inserts the tool and tries to grab the object stuck inside the SG. The success rate of these attempts varies and depends mostly on the skill of the operator of the FOSAR tool and experience. If an object is retrieved, a detailed analysis is conducted to determine its origin and structure. If the attempt fails, the location is reported and ECT inspection of the contact and surrounding tubes is performed at the shortest possible interval. Some objects are monitored during the entire time of operations in the SG's.

VI. Results

6.1 Introduction

The results of mechanical and chemical cleaning of the Krško NPP steam generators in the outage of 2019 are satisfactory, particularly in terms of the amount of removed sediment: 223 kg out of an estimated 290 kg. The estimation included total sludge inventory in the tube sheet area up to a height of approximately 1m. However, we can be less satisfied with the fact that we have not been able to clean both top-of-tube sheets (TTS). After the finished activity and "Lessons learned" we can now summarize the influencing factors, good and bad experiences, and give an evaluation of performance.

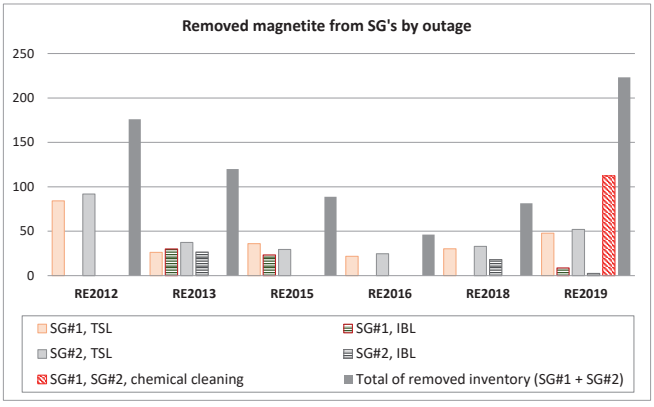

Fig. 7: Balance sheet of removed magnetite from SG's since 2012

Robert Kelavić, Marko Turalija, Mechanical and 1st Chemical Cleaning of NEK Steam Generators, Journal of Energy, vol. 71 Number 2 (2022), 10–17
https://doi.org/10.37798/2022712413

6.2 The short duration of the chemical phase (minus grade)

In October 2018, the length of the chemical cleaning activity was set based on the maximum length of the planned outage which was 28 days. At that time, the planned duration of the chemical phase was 80 hours, although the contractor's recommendation was from 100 to 110 hours. In addition, the "Performance Test" was performed at a time of t ≈ 100 hours. Due to other interconnected activities such as SL, IBL, VT, and FOSAR, no additional time was available in the overall Outage Plan.

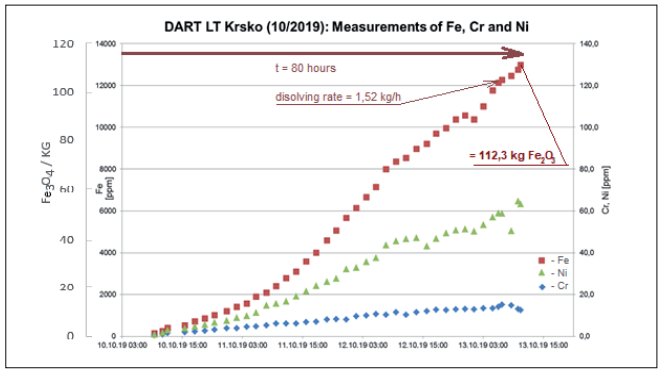

Fig. 8: Concentration rate of Fe, Cr, and Ni in EDTA solution during NEK application

At the moment when the dissolving rate of Fe was 1.52 kg/h, we discussed the possibility of process extension. The contractor proposed to extend it to 94 hours, which would provide 6 hours of "Safety margin" based on the 100-hour "Performance Test" qualification. We organized a meeting to extend the activity on the critical path, but during the meeting trend slowed down and the additional extension time was not agreed upon. Assuming that the chemical cleaning phase was prolonged, likely another 25 kg of Fe or more would be dissolved (1.36 x 25 = 34 kg Fe_3O_4). This would further improve the overall balance and reduce the hard deposits area. It should also be noted here that the amount of dissolved Ni and Cr was much lower in the chemical treatment than in the Qualification Performance Test, which means that there was no significant impact on the materials or systems.

Table 1

Removed sludge balance sheet

Removed sludge balance sheet (SG #1 & #2 in R´19 /out of 290 kg estimated)		
	SG #1 [kg]	**SG #2 [kg]**
1. SL		32,65 (before C.C.) *
Chemical cleaning ∑ (SG#1 + SG#2)	112,3	
1. SL	18,18 (after C.C.)	
IBL	8,598	2,536
2. SL	29,663	19,342
∑ (SL+IBL)	56,445	54,528
Mechanical cleaning ∑ (SG#1 + SG#2)	111,0	
∑ (CC + MC)	**223,3**	

* Since SL was performed on SG #2 before CC, it is believed that was the reason for an overall cleaner TTS on SG#2

6.3 Chemical composition of soft and hard sludge and influence on the chem. dissolution rate (minus grade)

2019 outage dissolutions of Fe or. Fe_3O_4 in EDTA solution was significantly slower and smaller in the site-implementation process than in the Performance Qualification Test under laboratory conditions at contractors' facilities, where previously removed (soft) sediment from the Krško NPP was used.

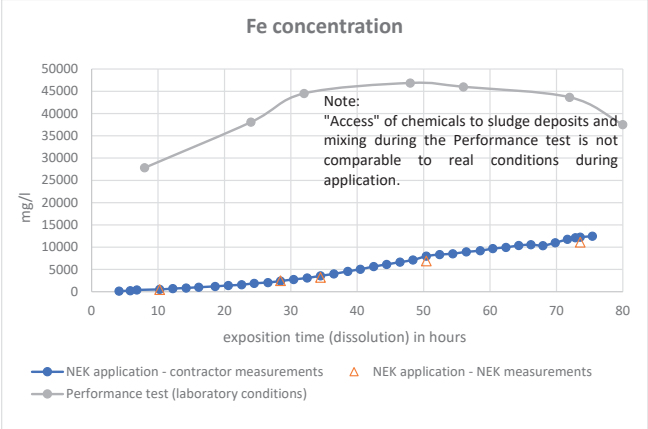

Fig. 9: The dynamics of real-life dissolution in the Krško NPP compared to the Performance Qualification test.

Some influential factors that have reduced solubility and slowed down the process can be identified:

- The hard sediment in the steam generator is compact, a kind of "concreted magnetite" that has been formed layer after layer since the replacement of SG's in 2000. Magnetite used in the "Performance test" was in the form of soft sludge like wet powder compared to hard sediment in the steam generator that had to be dissolved layer after layer again. The process was therefore slower and less efficient than in the laboratory.
- Mixing the medium in a laboratory autoclave was much more efficient than with the actual process in steam generators, where the tube bundle represents a large hydrodynamic flow resistance. Kinetics of a chem. reaction in the steam generators was, therefore, smaller and the process slower.
- The chemical composition of soft sludge is not the same as that of hard sediment. The presence of silicon (Si) and aluminium (Al) is known to have a negative effect on the dissolving of magnetite because it promotes the formation of highly resistible deposits. The last exact chemical composition of sediments is from the outage of 2012. The Si content increased from 2004 (the first analysis of sludge morphology) to 2012. Al in sediments (2004, 2006, 2009, and 2012) has not been reported.
- The laboratory can efficiently control the temperature during the whole process whereas the real-life application experiences some variations during this time.

6.4 Comparison of SG #1 and SG #2 cleaning sequence (plus SG#2 assessment)

Due to the outage plan and the fact that SG #2 was available earlier, the cleaning sequence started before SG #1. The proposal to start with SL (Sludge Lancing) was accepted, so the sequence of activities on both was a little different, which in the end contributed to a more efficient sludge removal on SG #2. The sequence of activities was:

Robert Kelavić, Marko Turalija, Mechanical and 1st Chemical Cleaning of NEK Steam Generators, Journal of Energy, vol. 71 Number 2 (2022), 10–17
https://doi.org/10.37798/2022712413

Table II

Comparison of SL1 between SG #1 and SG#2 before and after CC

Comparison of SL1 between SG#1 and SG#2 before and after CC		
	SG #1 (kg)	**SG #2 (kg)**
1. SL (Sludge Lancing)	18,184 (after C.C.)	32,650 (before C.C.)

From the large amount of soft sediment removed on SG #2, it was be concluded that on SG #1 a chemical dissolution of soft sludge took place which could have been removed by SL if the sequence of sludge removal was the same as on SG #2. Based on chemical principles and kinetics, the chemical reaction of dissolving the soft granulate* is faster, rather than the hard layers of magnetite, which at that time were mostly covered with soft sludge. Access to hard sludge to EDTA was severely restricted and this is the reason that the chemical dissolution of hard sediment at SG #1 was not as effective as at SG #2. Basically, at SG #1, we believe we used a chemical process to remove a lot of soft sludge that would be easier to remove with SL. Therefore, the final mass of sludge was smaller. (Soft granulate*: a mixture of dust and small moving particles of soft sludge of different sizes on the TTS).

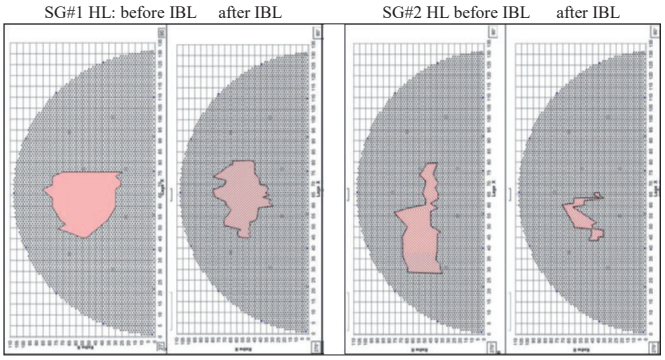

Fig. 10: Hard sludge deposits on Hot Legs of SG#1 and SG#2 before and after IBL

The surface area of hard sludge at the top of the tube sheet (TTS), which is a basic precondition for the formation and progression of the denting mechanism, decreased largely on SG #2 than it did on SG #1 after all removal activities. We expected similar sludge removal efficiency on both SG's but the distinction in the sequence of the mechanical and chemical cleaning process is probably the reason for the resulting differences.

6.5 Scraping / peeling off of brittle scales on SG tubes (plus grade)

Before the final VT (visual inspection) of the tube sheet, where foreign bodies were registered and the size of the area with hard sludge was determined, the plan was to dry the tube bundle with hot air as in previous outages. As a result of drying, peeling of a thin layer of hard scales on the tubes occurred. This is probably due to a combination of chemical cleaning and later hot air drying, which led to an uneven expansion of the scaling material and tubes of the steam generator (Figure 5). The result was a large amount of magnetite "scales" that were washed into the BD system and not taken into account in the final mass balance of removed sludge.

Fig. 11: Fallen scales of magnetite after SG drying phase

6.6 Appearance of a large number of foreign objects and their classification (plus grade)

Chemical cleaning was used to dissolve the hard sludge at the top of the tube sheet, which also revealed some foreign objects that were in deeper layers and had never been discovered before. The number of foreign objects is high, but most of them are thin wires that probably belonged to a wire brush.

Due to their weight and size the discovered foreign object are non-dangerous (classification: Type 1 / Category 3; Foreign Object Classification), but they leave a bad impression and they will have to be monitored in the future. If the process of accumulation of hard sludge continues, it will "disappear" over time. Their removal is not necessary and would often be technically impossible or at least very complicated and time-consuming.

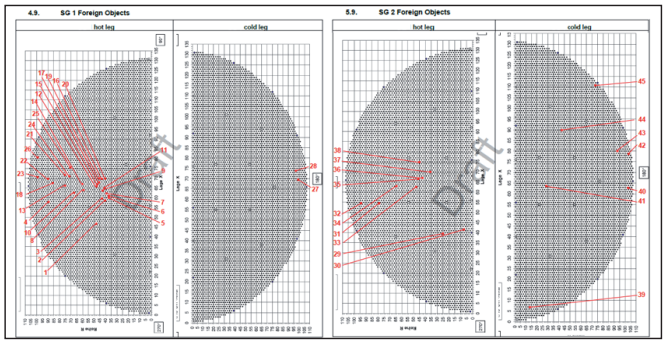

Fig. 12: Foreign object placement after outage 2019

Robert Kelavić, Marko Turalija, Mechanical and 1st Chemical Cleaning of NEK Steam Generators, Journal of Energy, vol. 71 Number 2 (2022), 10–17
https://doi.org/10.37798/2022712413

Limiting Object Categories[1,6]

Classification Type Number	Object Type Classification	Category 2 (Medium) Acceptable Object Dimensions (inch)[2]	Category 3 (Low) Acceptable Object Dimensions (inch)[2]
1	Wire[3]	2.5 long x 1/16 dia	1.75 long x 1/16 dia
2	Rod[4]	2.0 long x 1/8 dia	1.5 long x 1/8 dia
3	Rectangular Metal Objects	1/2 x 1/8 x 1/8	1/4 x 1/8 x 1/8
4	Machine Turning	1/2 x 1/8 x 1/8	1/4 x 1/8 x 1/8
5	Gasket[5]	1.75 long x 1/4 x 1/8	1.25 long x 1/4 x 1/8
6	Machine Remnant	1/2 x 1/8 x 1/8	1/4 x 1/8 x 1/8
7	Sludge Rock	1 x 1/4 x 1/4	3/4 x 1/4 x ¼ Or any size if soft or crumbles
8	Balls	1/2 Dia	3/8 Dia
9	Scale	-	Any size if soft or crumbles
10	Wire Bristle	3.0 inch Long 1/32 dia. - If small number found (no clumping found)	2.0 inch Long 1/32 dia. - If small number found (no clumping found)

[1]These object sizes are representative object dimensions based on two operational cycles or three years of plant operation. Actual part geometry, location, orientation and configuration may result in a more aggressive object and, therefore, would require a corresponding change to a higher priority.
[2]These sizes are based on finding the object in the annulus or on the tubesheet behind a tube. If the object is wedged between the tubes, it should be removed or a detailed engineering evaluation performed.
[3]Wires are semi-flexible objects.
[4]Rods are stiff objects.
[5]Assumes the object is lying flat against the tube.
[6]Sizes applicable for objects not located in red exclusion zone.

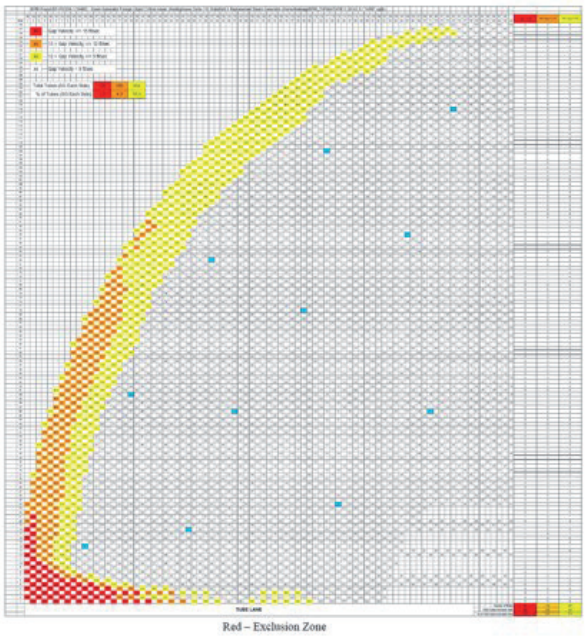

Fig. 13: Classification of foreign objects and the area of high hydrodynamic flow at the periphery of the SG tube bundle - EPRI summary SGMP TR 1020989

6.7 Chemical waste from completed chemical cleaning activity (plus grade)

At benchmarking at Asco NPP in Spain, information was received on the huge quantities of waste chemicals left in the yard after the activity was completed. This was mainly because the waste water showed traces of contamination and the recovery of the waste was not clearly defined in the contract. Therefore, we have included in the technical specification for procurement of the chemical cleaning activity that the contractor is responsible for the recovery and disposal of waste materials. The waste water was not contaminated in our case, so there were no problems in this area. The subcontractor took care of the rapid removal of chemical waste, which also avoided formal complications due to legal requirements for longer storage of this type of waste.

6.8 Removal of hard sludge in the area of DNTs from SG ECT R'18 and ECT reevaluation (2006, 2012, 2018), (SG #1 - minus grade, SG #2 - plus grade)

The primary goal of chemical cleaning was to clean the hard sludge area on the TTS under which the formation of the DNTs is taking place. After the 2018 outage, the ECT data from previous outages was reevaluated to determine when the denting mechanism appeared and with what dynamics it evolved. Statistical analysis of the data revealed that they were most extensively produced in the period 2006-2012, some of them even earlier. By evaluation of 2021 ECT data, it will be able to estimate the combined impact of 2 operational cycles, i.e. OL30 and cycle after chemical cleaning; OL31. Expectation is that we will not notice any progression on the dents around which the ″hard sludge″ has been removed.

Dent re-evaluation statistics also show large difference between the two steam generators. Therefore, it is best to comment on each one individually, but at the same time, it is necessary to evaluate the success of chemical cleaning in the critical area (hard sludge area) where the dents appear, because this can already predict the development or stagnation of this degradation mechanism.

6.8.1 SG #1 Hot Leg

ECT SG #1 in 2018 detected 33 dents on HL, which is essentially a small number based on the size of the ″hard sludge″ area. Interestingly, the 2006 denting mechanism was more developed at SG #1 (29) than at SG #2 (12). Nevertheless, the increment of a new dent at 6 cycles (2006-2012) was lower at SG#1. The right picture of the tube sheet shows the remaining ″hard sludge″ area after the 2019 chemical cleaning. The 2018 dent population has remained trapped in this area, which is not good. Optimistic about SG #1, however, is the fact that we only have 33 dents and that there were no new ones from 2012 to 2018. Since almost all dents have remained in the hard sludge area, we have to say that chemical cleaning on SG #1 HL did not fulfill expectations.

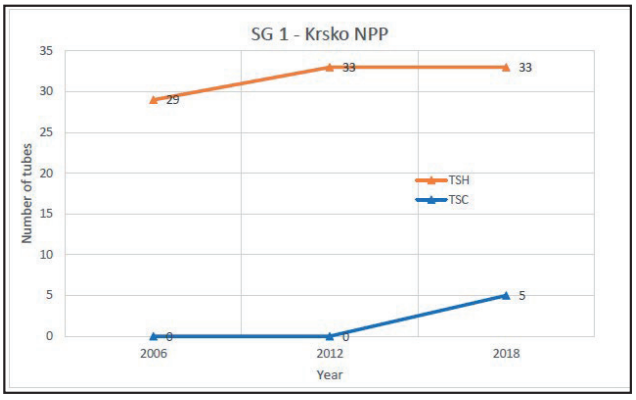

Fig. 14: Hard sludge area and DNT's after CC in SG #1 HL

Robert Kelavić, Marko Turalija, Mechanical and 1st Chemical Cleaning of NEK Steam Generators, Journal of Energy, vol. 71 Number 2 (2022), 10–17
https://doi.org/10.37798/2022712413

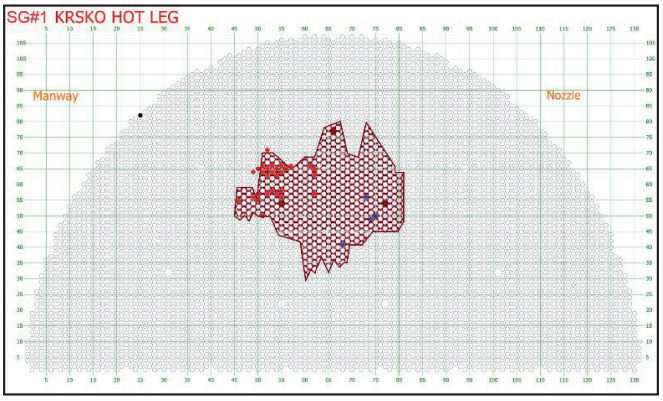

Fig. 15: Dent evolution on SG #1 HL (2002-2018)

6.8.2 SG #2 Hot Leg

ECT SG#2 in 2018 detected 83 dents on HL, 2.5 times higher than SG #1, although the hard sludge areas were comparable in size. The denting mechanism started slower than at SG #1, and its result is higher than at SG#1. Chemical cleaning was much more successful at SG #2 because it cleaned > 70% of the area in which the 2018 dents are located. This is far more important because the number of dents at SG #2 is much higher (83) as per SG #1 (33). It is here that we expect that the degradation mechanism will not develop further.

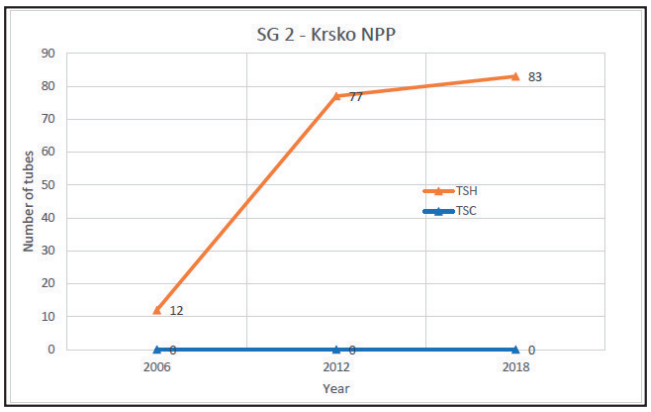

Fig.16: Hard sludge area and DNT's after CC in SG #2 HL

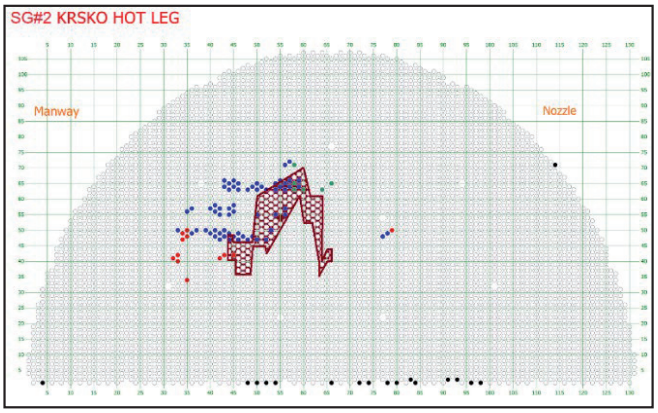

Fig. 17: Dent evolution on SG #2 HL (2002-2018)

With the projects implemented in the past cycle and the results, we have reached a much higher level of understanding of the degradation mechanism of denting, yet we still cannot explain why:

- more dents were generated on SG #2 (83) than on SG #1 (33),
- the number of the newly created dent was lower at SG #1 (4) than at SG #2 (65), in the period from 2006 to 2012
- the rate of newly formed dents decreased on both SG #1 (0 new) and SG #2 (5 new) in the period from 2012 to 2018

Evaluation of 2021 ECT data should provide some new answers. At that time, we will also be re-evaluating the dents from the second set of 50% ECT volumes (2021 – 2015 – 2009 – 2003). For the first time, we will also review the entire dent population - in the 100% scope in the same outage. This data will allow a final assessment of chemical cleaning, as well as an answer to whether the denting process has slowed down or even stopped. Should the trend continue or become even more intense, we can seriously think of repeating such a campaign.

At the moment, the results of statistics and predictions are not too pessimistic. In addition to that, some improvements are also planned that should make a positive contribution to water quality which supplies the FW system of steam generators. The final answer to the question of whether we need to do chemical cleaning in the area between the tube sheet and the first support plate again will be known after the following outages.

VII. Conclusion

In conclusion, the combined chemical cleaning and mechanical cleaning process met the expectations regarding the mass of sediment removed: 223 kg from an estimated 290 kg. The extracted amount equals to 77 % of the estimated, although the NEK goal was set around 80-90 %. The incomparable cleanliness of the hard sludge area especially on SG #2 was satisfactory which shall have a positive effect on the dent growth in the future. For SG #1 HL, the combination of the two cleaning methods fulfilled our expectation to some degree as we expect that due to the difference in the cleaning sequence the results were more visible on SG #2. Additionally, the CL sides of both steam generators were sufficiently cleaned as well. The most negative contributing factors that reduced Chemical Cleaning effectiveness were:

1. Short running time of the chemical cleaning phase (performed in t = 80 hours, which would require t ≥ 100 hours or more).
2. Activity sequence plan: likewise, on SG#1 the activity sequence should start with SL (Sludge Lancing), as it was with SG#2.

References

[1] NEK, "Efficiency Assessment of SG's – Sludge Lancing, Inner Bundle Lancing & Chemical Cleaning Activities During the Outage 2019 In NPP Krško", January 2020.

[2] "Replacement Steam Generator Assessment Study" Reference number: D02ARV01145105, rev. B, July 2019

[3] "Technical Description SL_VT_IBL_FOSAR" Reference number: F.031071-B-02, February 2019

[4] "DART LT NPP Krško 2019 - Final report" Reference number: D02-ARV-01-149-781, rev. A, December 2019

[5] "MC Technical Document for Final Report" Reference number: D02-ARV-01-149-200, rev. B, December 2019

[6] NEK CC project materials, July 2018 till December 2019

Journal of Energy

VOLUME 71 Number 2 | 2022

journal homepage: http://journalofenergy.com/

Determining the Transmission Capacity of Existing Transmission Lines Under High Wind Generation Conditions

Ivan Pavičić[1], Alan Župan, Marija Žmire, Ninoslav Holjevac

Summary — Determining the transmission capacity of existing transmission overhead lines (OHL) is primarily defined by conductor ampacity. Transmission OHL needs to be loaded with the currents below their thermal capacity limit to avoid irreparable damage to conductor. The maximum value of current can be determined by the static approach (STR – Static Thermal Rating) or by the dynamic approach (DTR - Dynamic Thermal Rating). STR is defined by simple calculations and often does not change throughout the year while the DTR is calculated in real time taking into account actual atmospheric conditions, weather forecasts and actual conductor current. Most common approach used to calculate conductor temperature is by applying IEEE standard (IEEE 738, 2012) or CIGRE standard (TB601, 2014). During the higher production from wind farms caused by, higher wind speeds, it can be the case that local transmission OHL are loaded up to their limits and congestions can occur. But in case dynamic approach of capacity estimation is used it can show that due to high wind speed and better heat removal conditions the actual capacity of the line might be higher. In this paper, analysis of relation between atmospheric parameters, wind speed, wind direction, ambient temperature and solar insolation, and ampacity is described. Considering historical weather data from meteorological stations, actual atmospheric conditions on transmission OHL corridors and taking into account the frequency of occurrence of individual meteorological variations ampacity of conductor is determined. For determined ampacity the potential variation and uncertainty of estimation is provided through different indicators. The obtained results provide an insight into the change of OHL ampacity based on actual conditions and their potential to be loaded even over their rated ampacity in cases of high engagement of wind power plants.

Key words — capacity of over-head transmission line, conductor ampacity, conductor temperature, meteorological conditions, ACSR conductor (Aluminium Conductor Steel Reinforced), dynamic thermal rating DTR

(Corresponding author: Ivan Pavičić)
Ivan Pavičić, Alan Župan, and Marija Žmire are with the Croatian transmission system operator (HOPS)
Zagreb, Croatia (e-mails: ivan.pavicic@hops.hr, alan.zupan@hops.hr, marija.zmire@hops.hr)
Ninoslav Holjevac is with the University of Zagreb Faculty of Electrical Engineering and Computing,
Zagreb, Croatia (e-mail: ninoslav.holjevac@fer.hr)

[1] Statements expressed in the paper are author's own opinions, they are not binding for the company/institution in which author is employed nor they necessarily coincide with the official company/institution's positions.

I. Introduction

Integration of large number of renewable energy sources into the power system potentially increases loading of some transmission OHL and can cause congestions is specific network segments. To avoid congestions it is necessary to consider possible solutions to increase the capacity of OHL and overall capacity of the transmission system. Construction of new transmission OHL can be challenging and depending on the circumstances can be economically unjustified. Therefore, different solutions to increase the capacity of existing OHLs are being considered. One of the ways to better utilize the existing OHL transmission capacity is to determine its actual, real time, operational ampacity in a certain moment based on measurements and actual weather conditions

OHL ampacity ratings determine the thermal limits of conductor and suspension equipment. During operation, it is necessary to respect the permissible thermal load that the equipment can withstand, to avoid incurring irreparable structural damage and loss of mechanical and electrical properties. In most cases operational ampacity is determined for most unfavorable weather conditions that can be expected on the transmission OHL corridor. This approach is called STR and can be defined for different periods of the year, for example winter and summer periods. Another approach is to determine ampacity limits of OHL in real time using DTR approach where operational ampacity is depending on the current weather conditions, most recent weather forecasts and on the actual status of the line [1], [2], [3].

Based on conducted studies determined operational ampacity highly depends on the speed of the wind and its direction. Wind is considered to be the dominant factor in process of dissipating heat from the conductor [4], [5], [6]. On higher wind speeds ($\approx$20 m/s) operational ampacity can theoretically increase up to 4 times compared to low wind conditions [7]. At the same time under the higher wind speed conditions there is a high probability of having a significant production from wind power plants. Applying DTR where OHL have to operate near their operational limits is considered and with different weather conditions is considered [8]. Using DTR involves complex methodologies that need to be investigated separately for each case/corridor and that need to be in accordance with legal and technical requirements [9].

This paper considers influence of weather conditions on capacity/ampacity limits of transmission OHL. Determination of the transmission OHL ampacity is conducted in accordance with the IEEE 736.2012 standard [10]. In section 2 standard models for calculating conductor temperature are presented. Influence of

Ivan Pavičić, Alan Župan, Marija Žmire, Ninoslav Holjevac, Determining the Transmission Capacity of Existing Transmission Lines Under High Wind Generation Conditions, Journal of Energy, vol. 71 Number 2 (2022), 18–22
https://doi.org/10.37798/2022712378

environmental weather parameters is carried out in section 3. For observed case study transmission OHL and historical measured weather parameters analysis of DTR is described in section 4 and conclusion is given in section 5.

II. Current Ampacity of OHL

Calculations of the maximum current can be done using one of the standards (IEEE, CIGRE or IEC) that take into account structure and design of the conductor, the meteorological conditions and the operating conditions of the transmission OHL [11], [12].

Based on the mentioned standards, determining operational ampacity for OHL in operation can be done using either using STR or DTR approaches. Applying STR approach takes into account the most conservative climate and weather conditions for observed OHL. In reality, this approach gives very conservative limits and can lead to lower level of OHL capacity utilization. On the other hand, the dynamic DTR approach takes into account current meteorological conditions (wind speed and wind angle, ambient temperature and solar insolation) at critical and most demanding segments of the OHL corridor and based on them, calculation of operational ampacity is performed. The fundamental principle for determining operational ampacity of a conductor is its heat balance between the heat generation and heat dissipation. For this reason, taking into account current meteorological conditions proves to be a more effective approach for determining OHL ampacity.

Calculating temperature of conductor is possible using several standard, where IEEE and CIGRE standards are the most represented. Both standards apply the heat balance of the conductor to calculate the temperature of the conductor, where the IEEE standard gives more conservative results compared to the CIGRE standard. The same CIGRE standard is more suitable for practical engineering based on simplified online monitoring of OHL parameters [12]. CIGRE transient thermal equation of the conductor (eq. 1) describes the dynamic temperature changes due to changes in conductor current and changes in meteorological conditions along the conductor route. Equation (eq. 1) describes the dynamic change in temperature caused by conductor and meteorological condition changes.

$$q_c + q_r + q_w + mC_p \frac{dT_c}{dt} = q_M + q_C + q_S + I^2 R(T_c) \quad (1)$$

Where q_c marks convective cooling, q_r radiative heat loss, q_w evaporative heat loss, $mC_p \frac{dT_c}{dt}$ heat capacity of the conductor with m being the mass per unit length, c_p specific heat capacity of conductor and T_c the theoretical conductor temperature, q_m magnetic heat, q_c corona heat loss, q_s solar heat and $I^2R(T_c)$ joule heat losses where I^2 being current and $R(T_c)$ conductor resistance at the given temperature.

IEEE standard transient heat equation of the conductor (eq. 2) describes the temperature of the conductor in a simpler form considering that certain effects are not always present and relevant and ultimately their amount does not significantly affect the final temperature of the conductor.

$$q_c + q_r + mC_p \frac{dT_c}{dt} = q_s + I^2 R(T_c) \quad (2)$$

Where again q_r radiative heat loss, q_c corona heat, $mC_p \frac{dT_c}{dt}$ heat capacity of the conductor, q_s solar heat and $I^2R(T_c)$ joule heat losses.

Observing the IEEE heat equation of the conductor it can be concluded that the temperature of the conductor primarily depends on two main factors: 1) the current passing through the conductor; 2) the meteorological conditions around the conductor (wind speed, wind direction, intensity of solar radiation and ambient temperature). Current measurement can be done at the beginning and at the end of the transmission line while measurements of meteorological conditions need to be done on critical segments along the transmission OHL corridor. When all parameters are known and the input parameters do not change, heating and cooling of the conductor are equal, i.e. thermal balance is achieved and previous equation (eq. 2) can be rewritten in simpler form (eq. 3):

$$q_c + q_r = q_s + I^2 R(T_c) \quad (3)$$

From equation above (eq. 3) conductor current can be calculated when all meteorological conditions are known (eq. 4.):

$$I = \sqrt{\frac{q_c + q_r - q_s}{R(T_c)}} \quad (4)$$

By calculating the abovementioned maximal current the operating transmission capacity of OHL can be directly determined. In most cases this DTR approach can lead to higher capacity compared to the STR calculated values, all under the assumption the voltage stability is also satisfied. In today's transmission networks active managing of transmission capacity through the process of determining its thermal limit can provide increased flexibility of operation.

III. Calculation of Maximal Current Using IEEE 738 Standard

3.1. Input parameters

When calculation is performed main parameters that affect conductor temperature can be divided into two groups, conductor parameters (conductor diameter, permissible conductor temperature, emissivity and absorption, altitude and latitude) and weather conditions (wind speed and wind angle, air temperature and insolation). All mentioned parameters depend on the conductor itself, the geographical position of the transmission OHL and meteorological data. Therefore the result of this calculation can differ significantly for each case and an individual analysis determining operational ampacity of conductor for each transmission OHL is necessary.

This paper considers influence of the meteorological conditions on transmission capacity of the OHL calculated in real time. More specifically the results are observed for specific grid segment in Croatian transmission grid for periods when the production from the surrounding wind farms is the highest. This occurs during summer period under the most unfavorable meteorological conditions. For the meteorological data input, measuring station on the transmission OHL pole at a height of 10 m from the ground was chosen. This specific measuring station is located in the forest basin which represents the most unfavorable meteorological conditions along the corridor. Observed transmission OHL is equipped with one conductor ACSR 240/40 mm^2 with conductor diameter 21,8 mm, ohmic resistance 0,12 Ω/km, emissivity of conductor factor 0,5 and solar absorption factor of 0,5. Maximum permitted temperature of the conductor is determined by national legislation and is equal to 80°C. Some of the manufacturers of the ACSR conductors state

Ivan Pavičić, Alan Župan, Marija Žmire, Ninoslav Holjevac, Determining the Transmission Capacity of Existing Transmission Lines Under High Wind Generation Conditions, Journal of Energy, vol. 71 Number 2 (2022), 18–22
https://doi.org/10.37798/2022712378

that the maximum permitted temperature for their conductor is up to 100°C, but the final value is defined by the customer regarding technical regulations and individual national legislation [13]. According to historical data collected from the selected measuring meteorological station on one-year period the following min and max values where recorded: wind speeds in range from 0 to 13.7 m/s and air temperature in range from -10.3°C to 37.2°C. For calculations, the wind speed and temperature are taken as mean value of 15-minute measured intervals. The insolation angle was divided into time series that changes from 0° at 12 o'clock and 15° for every hour after noon.

3.2 Influence of input parameters on OHL ampacity

Heat generation of conductor is primarily consequence of the current passing through the conductor and solar insolation. Conductor's temperature will be higher than ambient temperature because of those effect so the thermal transmission will always be present between conductor and ambient air. It can be said that environment around conductor is acting like energy sink for generated heat in conductor. Therefore, environmental conditions have a decisive impact on the final temperature of the conductor. Maintaining conductor temperature below permissible thermal limits is the main goal and it is achieved by understanding the thermal balance of the conductor. Main physical processes responsible for the cooling effect are convective and radiative cooling, where convective cooling is provided by air flow (wind) and radiative cooling occurs as a result of heat emission without physical contact caused by temperature difference. In order to understand the influence of the mentioned parameters on the permitted current, calculations were carried out for a selected ACSR 240/40 mm^2 conductor. Initial input data that was taken for test case calculation include ambient (air) temperature 40°C, wind speed 0,6 m/s, wind angle 90° and maximal solar radiation (161th day of the year, at 2 p.m), emissivity and absorption factor 0,5 for the maximal conductor temperature 80°C. Results of conducted calculation are mainly theoretical and can be applied in most cases. Calculation was conducted using the programmed script that was developed based on Annex - A IEEE standard [10].

The convection heat loss of OHL highly depends on the angle and wind speed. Therefore it is represented by a complex calculation for forced cooling with the presence of wind of different speeds compared to the case without the presence of wind where natural cooling is dominant. For calculation based on IEEE standard it is possible to determine the heat transfer for all wind speeds and consequently the conductor current at 80°C. Obtained results for different wind speeds are shown in Figure 1. For increase of wind speed in steps of 2.5 m/s it can be seen that characteristic is not linear and that the most significant maximal current increase is achieved at low wind speeds. For a wind speed from 0 to 5 m/s, there is an increase in the current by 160%, and for an increase in speed from 5 to 20 m/s, there is an increase of the current by additional 51%, while the total increase in the current is 293%. The influence of the wind direction on the allowed current is also shown on Figure 1. Again, a non-linear characteristic is visible. For a wind angle of up to 7° there are no changes/increases, while for a wind angle of 40° there is an increase in the maximal allowed current by 33%. Finally for an additional increase in the wind angle from 40° to 90° there is an increase in the current by another 10%, with the total current increase summing up to 46%.

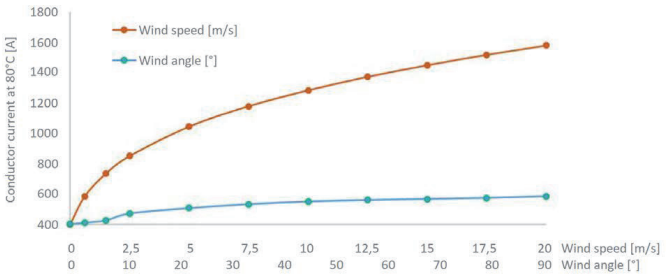

Fig. 1. Conductor allowed current at 80°C depending on different wind speeds and wind angles

Conducting heat from conductor to the environment is mainly influenced by the temperature of the surrounding air. The lower air temperature and consequently greater temperature difference between conductor and surrounding air leads to better convection and radiation of heat. Figure 2 shows the influence of temperature of the surrounding air on the maximal allowed current, where for the observed air temperature range is 0°C to 40°C. From the Figure 2 it can be seen that the curve is approximately linear. For the observed temperature range of surrounding air (0°C – 40°C), the current is reduced by 52% at 40°C compared to current 0°C.

The calculation of solar heat (insolation) influence on conductor temperature was also considered. With an increase of insolation in range from 0 to 1000 W/m^2, conductor absorbs more energy that contributes to an increase in its temperature. Influence of insolation on conductor temperature is shown on Figure 2. It is evident that, as is the case of an increase of temperature, that the function is dominantly linear. For the selected sunniest hour of the year (161st day of the year at 14 hours), which corresponds to the maximum radiation, a reduction of the permitted current load of 8% can be expected compared to the case of solar radiation intensity of 0 W/m^2.

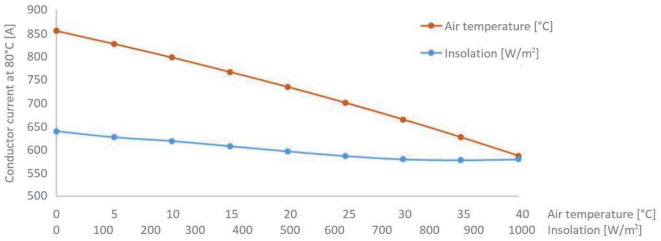

Fig. 2. Conductor allowed current at 80 °C dependence on air temperature and insolation

Conducted calculations were done separately for each parameter that was changed while the other parameters were constant (Ceteris paribus approach). In real operation this is not the case. In section 4 analysis for real conditions will be conducted taking into account changeable weather condition. Conducted calculation shows that wind speeds have dominant influence on conductor temperature and due to wind characteristics often demonstrating rapid changes permissible current can be significantly affected. Wind angle has similar characteristic like wind speed with rapid changes in while ambient temperature is relatively stable with slower changes throughout the course of the day. Insolation usually has similar characteristic like temperature demonstrating gradual changes, but can also have steeper changes due to sudden appearance of clouds or storms. Through presented analysis of Section 3 from all the input parameters analyzed wind speed and angle have been concluded to have dominant influence with air temperature and insolation influence being less impactful.

Ivan Pavičić, Alan Župan, Marija Žmire, Ninoslav Holjevac, Determining the Transmission Capacity of Existing Transmission Lines Under High Wind Generation Conditions, Journal of Energy, vol. 71 Number 2 (2022), 18–22
https://doi.org/10.37798/2022712378

IV. Calculating Dynamic Transmission Capacity of an OHL

For the described calculations in this Chapter 4, conductor is defined by its final and unchanged model and conductor current depends primarily on the weather conditions. Atmospheric and meteorological conditions are different throughout the year and it is desirable to determine a characteristic for each period that is observed. In conducted analysis both STR and DTR approach were used where STR values are defined for unfavorable atmospheric conditions where ambient (air) temperature is 40°C, a wind speed of 0.6 m/s, maximum solar heat and maximum conductor temperature of 80°C. For presented conditions calculated STR approach maximal current is 605 A.

In the process of calculating currents with DTR approach, available real time measured meteorological data is necessary, as well as forecasted values for corridor segments not covered by installed measurement devices. In the previous chapter influence of various atmospheric conditions were presented where highest ampacity was achieved for higher wind speed values that appear just in a small number of hours for the observed period and are therefore not realistic for practical use. Differences in environmental conditions change significantly throughout the year where higher transmission capacity of OHL are achieved in winter, when the ambient temperature and solar radiation are the lowest and the wind intensity is statistically the highest. In order to get a realistic insight into the ampacity of OHL analysis was performed for time period of high air temperatures, high solar radiation and high wind, consequently also high production from the surrounding wind farms. Third week in June (from June 16, 2021 until June 2021) was selected. Based on presented calculation in section 2 conductor current (at conductor temperature 80°C) were calculated for each 15-min interval and the results are shown on Figure 3.

Conducted calculation for the mentioned period shows an average increase in transmission capacity of OHL by 9%, while the recorded maximum increase was 45% compared to STR values. Also using DTR there were periods with lower values of transmission capacity with recorded minimum of 25% smaller capacity compared to STR calculated limit due to low wind speed and bad wind angle. From Figure 3, where the curve of the calculated maximum current is shown for both approaches, it is also evident that the lowest values were achieved when the wind speed and consequently production from wind farms were the lowest. For these specified hours where DTR current value is lower than STR an additional analysis is required to determine the influence of atmospheric parameters contribution to lower ampacity result.

For the intervals where the DTR current values were calculated below the STR value analysis was made for wind speed and wind direction as limiting input parameters. In relation to the STR calculation of the current, which assumes a wind speed of 0,6 m/s and a wind angle of 90°, a total of 186 15-minute intervals (out of a total of 672 intervals) were recorded in which the calculated current was lower than the nominal STR value.

Table 1 shows the distribution of recorded 15-min intervals (for different groups of calculated current I_{Cal} where I_N represent the nominal STR value. The main causes for smaller value of I_{Cal} compared to I_N are the differences in wind angle and wind speed. Based on the results from Table 1, it can be concluded that the wind speed significantly affects the lower values of the I_{Cal} ($I_{Cal} < 0{,}9\ I_N$), while the wind angle is significant in all calculation of the I_{Cal}. The main causes of the lower value I_{Cal} compared to I_N comes from the fact that I_N was calculated for wind speed 0,6 m/s and wind angle of 90° where in reality there were period with lower speed (below 0,6m/s) or without wind and with lower wind at lower angle.

Table 1. The distribution of intervals for which is $I_N > I_{CAL}$

I_{Cal} [A]	Intervals		
	$I_N > I_{Cal}$	Wind speed <0,5 m/s	Wind angle <60°
$0{,}7\ I_N < I_{Cal} < 0{,}8\ I_N$	5	60%	100%
$0{,}8\ I_N < I_{Cal} < 0{,}9\ I_N$	58	45%	95%
$0{,}9\ I_N < I_{Cal} < I_N$	123	20%	86%

Additional analysis also considers conductor temperature for the most unfavorable case recorded where $I_{Cal} < I_N$ and with input

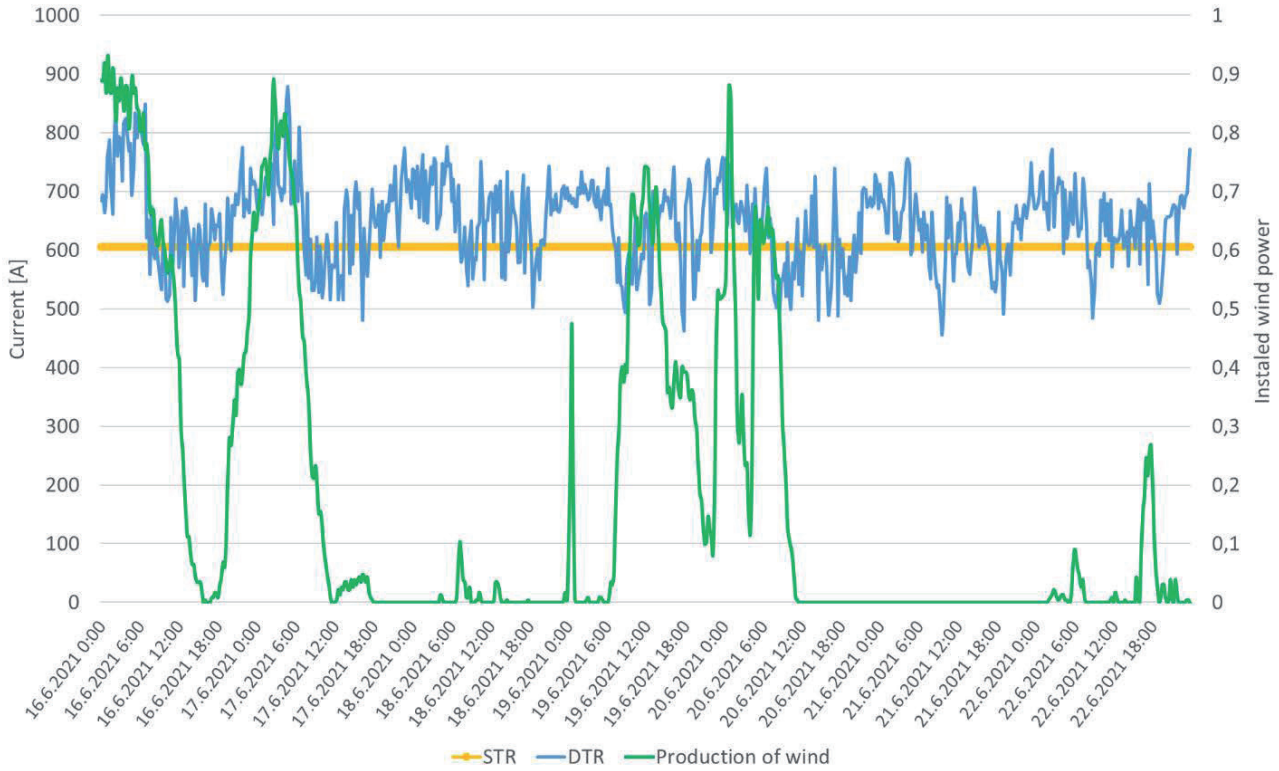

Fig. 3. Comparison of DTR (blue) and STR (yellow) current conductor with the wind generation output in the area (green)

Ivan Pavičić, Alan Župan, Marija Žmire, Ninoslav Holjevac, Determining the Transmission Capacity of Existing Transmission Lines Under High Wind Generation Conditions, Journal of Energy, vol. 71 Number 2 (2022), 18–22
https://doi.org/10.37798/2022712378

data: wind speed 0.3 m/s, air temp. 28°C, wind angle 16° at 9 am. For these conditions calculated conductor temperature was 99.7°C. Taking into account the recommendations of the conductor manufactures for the permanent temperature of the ACSR conductor (up to 100°C) [13] without loss of mechanical properties, it can be concluded that the design current values were not exceeded at any time for observed period.

Finally, it can be concluded that during high wind generation the transmission capacity of OHL is increased compared to the nominal STR values. The increased values directly depend on the current meteorological conditions on the transmission OHL and the location of the transmission OHL in geographical place in relation to the wind power plants. In the moments when lower transmission capacity of transmission OHL compared to STR values was recorded, no significant production from wind farms was present due to lower wind speed which makes the lower ampacity result less impactful. On the other hand, during high production of wind when high loading of the grid is expected the DTR calculated ampacity is higher which can significantly impact the power flows and transmission system operation.

V. Conclusion

In process of determining transmission capacity of OHL various methods can be used to calculate maximum current. OHL ampacity in real time can be done using different standards where IEEE and CIGRE are most represented. Calculations of OHL maximal current are highly influenced by atmospheric parameters. It can be expected that similar atmospheric condition are presented on local geographical area and in the case of higher wind generation transmission capacity of OHL can significantly depend on wind speed and angle. The results show that STR approach is conservative and applying DTR can effectively increase OHL capacity, especially during times of high wind and consequently high wind production. Presented calculation of OHL ampacity by DTR approach compared to STR values were made for most unfavorable week in year and still the conclusion drawn was that there is a high correlation between the need for higher OHL capacity due to higher wind generation evacuation and simultaneously higher calculated DTR capacity at these moments.

In future work, the uncertainty of system power flow analysis and the operational risk of transmission capacity will be investigated. Also, in that regard conducted analysis shows promising results since it could provide more efficient process for determining transmission capacity and can be applied in the business processes of planning and management of the transmission grid.

References

[1] B. Nemeth, V. Lovrenčić, M. Jarc, A. Ivec, M. Kovač, N. Gubeljak, U. Krisper, "Advanced prevention against icing on high voltage power lines", vol. 67 no. 2 (2018): Journal of energy Energija

[2] V. Lovrenčić, M. Krevelj, M. Kovač, „Dinamički temperaturni monitoring nadzemnih vodova prijenosnog sustava", 10. simpozij o sustavu vođenja EES-a, Opatija 2012

[3] K. Adomah, Y. Mizuno, K. Naito, „Examination of CIGRE method of assessing transimsssion line conductor's temperature", T.IEE Japan, Vol. 121-B, No. 6, 2001

[4] Antoulinakis, F.; Chernin, D.; Zhang, P.; Lau, Y.Y. „Effects of temperature dependence of electrical and thermal conductivities on the Joule heating of a one dimensional conductor", International Conference on Plasma Science (ICOPS), Denver, CO, USA, 19–23 June 2016.

[5] Sidea, D.; Baran, I.; Leonida, T. „Weather—based assessment of the overhead line conductors thermal state", Eindhoven PowerTech, Eindhoven, The Netherlands, 29 June–2 July 2015.

[6] Group of authors, „Review of Thermal Stress and Condition Monitoring Technologies for Overhead Transmission Lines: Issues and Challenges", IEEE Access, July 2020.

[7] Fan S., Yanling W., Lei. Z., Kun Q., Likai L., Zhijun Y., Weihau T., „Study on Thermal Load Capacity of Transmission Line Based on IEEE Standard", Journal of information processing systems (JIPS), June 2019.

[8] Martinez, R.; Manana, M.; Arroyo, A.; Bustamante, S.; Laso, A.; Castro, P.; Minguez, R. Dynamic Rating Management of Overhead Transmission Lines Operating under Multiple Weather Conditions. Energies 2021, 14, 1136. https://doi.org/10.3390/en14041136

[9] Group of authors, „Operational aspects of dynamic line rating. Application to a real case of grid integration of wind farms", Cigre B2-105, 2016

[10] IEEE 738 Standard, "IEEE Standard for Calculating the Current-Temperature Relationship of Bare Overhead Conductors", 2013.

[11] [CIGRE, "CIGRE Guide for Thermal Rating Calculations of Overhead Lines", Paris, France, 2014.

[12] [Staszewski L., Rebizant W., "The Differences between IEEE and CIGRE Heat Balance Concepts for Line Ampacity Considerations", Modern Electric Power Systems, Wroclaw, Poland, 2010

[13] available online, accessed online on 27th February 2023, https://www.entsoe.eu/Technopedia/techsheets/high-temperature-low-sag-conductors-htls

Journal of Energy

VOLUME 71 Number 2 | 2022

journal homepage: http://journalofenergy.com/

MELCOR-To-MELCOR Coupling Method in Severe Accident Analysis Involving Core and Spent Fuel Pool

Hector Lopez, Alessandro Petruzzi, Walter Giannotti, Domenico De Luca

Summary — A lot of effort has been spent to prevent the occurrence of SA in nuclear plant and to develop Severe Accidents (SA) Management to mitigate the consequences of a SA. Those consequences are mainly related to limit the release of fission product to the environment. The core in the vessel is not the only source of fission products as the Spent Fuel Pool (SFP) hosting the fuel removed by the core is, in some NPP, inside the containment and SA conditions can also occur. This is especially important in reactors having proximity between the RPV and SFP such as the VVER-1200. This close proximity implies that any SA occurring in the SFP potentially affects the RPV and vice-versa. This potential combination might cause unexpected evolution in the SA progression to whom the safety systems are not able to contain. MELCOR code is a widely used, flexible powerful SA code but it is incapable (due to the uniqueness of the COR package use inside the same input) to reproduce a situation in which both the fuel in vessel core and the fuel in the SFP, inside the same containment, are going to experience a severe accident scenario. The current study presents a MELCOR-to-MELCOR coupling method to simulate simultaneously scenarios with both, core and SFP, as sources capable of H_2 generation, fuel damage and FP release in a VVER-1200 NPP. The coupling is performed by running two simulations in parallel and with the data exchange supervised and managed by a dedicated Python coupling supervising script developed at NINE.

Keywords — **MELCOR, SA, severe accident, spent fuel pool, coupling, VVER-1200**

I. Introduction

In Severe Accidents (SA) Management, the main target is to avoid the release of fission products to the environment and to limit the dose to the population that is the general regulatory safety requirement. A lot of effort has been spent to manage the consequences of the core damage constituting the begin of the SA phase in the accident progression. However, the core in the vessel is not the only source of fission products in the containment as the Spent Fuel Pool (SFP) hosting the fuel removed by the core is, in some NPP, inside the containment and SA conditions can occurs in the pool.

An effect of the occurrence of a SA in the SFP is the intensive generation of H_2 due to the heat up and oxidation of the rod cladding if the coolant inventory is lost or if system providing cooling to the pool fails. The impact of the H_2 is enhanced by the fact that the spent fuel pool releases H_2 directly in the containment leading to scenarios with large amounts of H_2 in the containment in early stages of the accident. An SA occurring in the SFP could potentially lead to the melting of the contained fuel rods leading to the damage of the structures in the containment. This is especially important in reactors having proximity between the RPV and SFP such as the VVER-1200. This close proximity implies that any SA occurring in the SFP potentially affects the RPV and vice-versa. This potential combination might cause unexpected evolution in the SA progression to whom the safety systems are not able to contain.

MELCOR is a fully integrated, engineering-level computer code developed at Sandia National Laboratories for the U.S. nuclear Regulatory Commission whose primary purpose is to model the progression of accidents till the SA phase in LWR NPPs. MELCOR code is capable to analyze a large spectrum of severe accident phenomena in both BWR and PWR. Although MELCOR is a widely used, flexible powerful SA code, it is incapable to reproduce a situation in which both the fuel in vessel core and the fuel in the SFP, inside the same containment, are going to experience a severe accident scenario due to the uniqueness of the COR package use inside the same input [1][2].

Initial attempts to circumvent this MELCOR limitation have been performed by using separate integral calculations with subsequent combination of individual core and SFP SA effects but this approach was not suitable to fully capture the interactions between the systems. Thus, a MELCOR-to-MELCOR coupling approach have been widely assumed to perform such calculations.

Previous studies on the implementation of MELCOR-to-MELCOR coupling method present documented examples of the use of the Parallel Virtual Machine (PVM) Message Exchange [3]. This virtual machine created by the executive program after reading the input monitors the information to be exchanged and coordinates the advancement through time.

Despite presenting promising results in the aforementioned studies [3], the main limitation with the use of the PVM is the requirement of the user having access to the MELCOR source code in order to link the PVM libraries with the code. This requirement makes the PVM unsuitable for the present study. Thus, the development of a new coupling method that does not require access to the source code was done in N.IN.E..

(Corresponding author: Hector Lopez)
Hector Lopez, Alessandro Petruzzi, Walter Giannotti, and Domenico De Luca are with the Nuclear and Industrial Engineering (NINE) Lucca, Italy
(e-mails: h.lopez@nineeng.com, a.petruzzi@nineeng.com, w.giannotti@nineeng.com, d.deluca@nineeng.com)

Hector Lopez, Alessandro Petruzzi, Walter Giannotti, Domenico De Luca, MELCOR-To-MELCOR Coupling Method in Severe Accident Analysis Involving Core and Spent Fuel Pool, Journal of Energy, vol. 71 Number 2 (2022), 23–28
https://doi.org/10.37798/2022712421

The paper is organized as follows. The description of the coupling method developed by Nuclear Industrial Engineering (N.IN.E.) is presented in Section 2. Section 3 show the proof of concept scenario designed to test the coupling and, the results of the aforementioned scenario are shown in Section 4. Lastly, the future work is described in Section 5.

II. N.IN.E. MELCOR-to-MELCOR Coupling

The basic concept of the coupling method consists into run two simulation models in parallel, each one representing a portion of the overall domain, with constant data exchange between them through the interface. Based on the previous definition two major elements are defined; the simulation models domains and the data exchange management. Both elements are described in this Section.

In case of a MELCOR-to-MELCOR coupling, each domain is defined by the aforementioned limitation of the code; the presence of a COR package. For the scenario of interest, the domains consist on the CORE domain which includes the RPV, cooling circuits and most of the containment system and the SFP domain which includes the fuel pool itself and the remaining part of the containment system. Each domain is assigned to a separate MELCOR calculation with dedicated input and different inputs COR package (the CORE and the SPF respectively). Figure 1 depicts the domains used for a VVER-1200 simulation model.

As mentioned above, the coupling method requires a constant data exchange between both domains in order to provide accurate results. Figure 2 shows the basic chart flow of the coupling method function. As the figures suggests through the red lines, on each time step, the data needed is extracted from the output of one of the files and sent to the input of the other file, which is modified accordingly with the new information received. After the data is exchanged between both domains, both calculations are repeated with the updated values until a convergence check is passed.

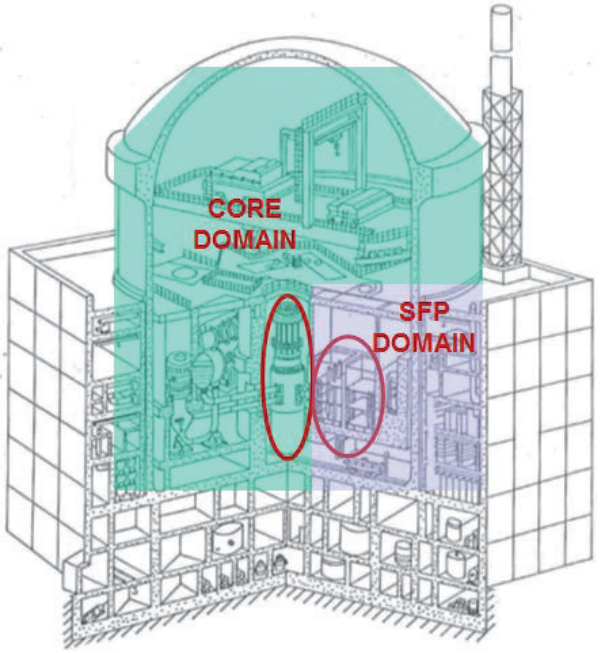

Fig. 1: VVER-1200 MELCOR-to-MELCOR Coupling Domains.

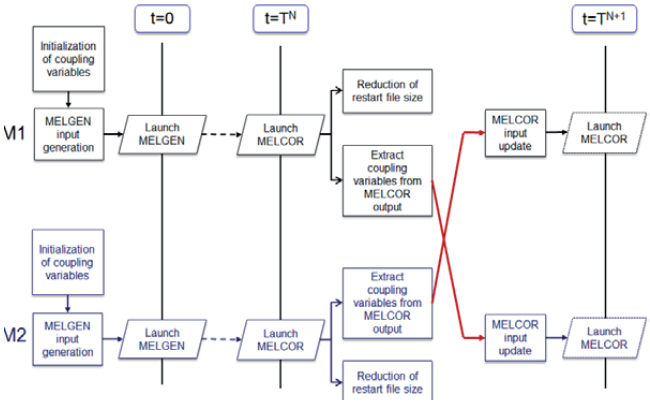

Fig. 2: N.IN.E. MELCOR-to-MELCOR Coupling Flow Chart.

Thus, how to manage the data exchange is a key element when developing the coupling. Weaver et. al. [4] describe the different coupling schemes used by RELAP and other codes. The most common coupling methods use either explicit or semi-implicit coupling schemes.

The first of the coupling schemes is the explicit scheme. In this methodology, although the data exchange occurs at the beginning of the time step, T^n, in both directions, pressures in the boundary volumes are held constant throughout the time step and only updated at the end. This condition causes the systems to be limited by the sonic Courant condition. Scenarios with larger Courant numbers will turn out in undesired oscillations in the results of the calculations. In addition, there is no control and correction of truncation error during the data exchange. Previous studies have proved this restriction (Aumiller et. al.) [5]. This restriction makes fully explicit coupling impractical. Figure 3 and Figure 4 show the data exchange of the explicit scheme diagram at a given time step.

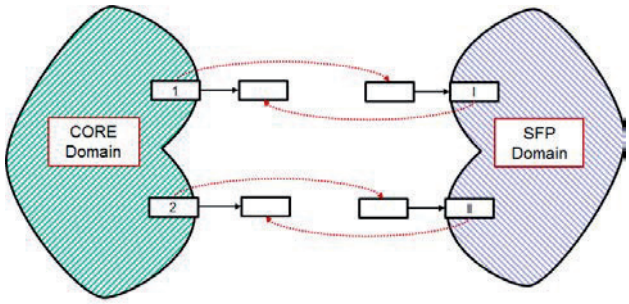

Fig. 3: Schematic of Explicit Coupling Methodology.

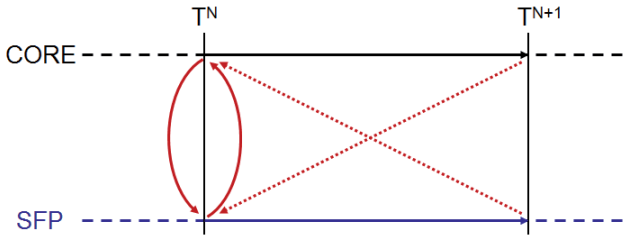

Fig. 4: Explicit Coupling Methodology Time Step Advancement.

The semi-implicit coupling scheme, on the other hand, uses a Master-Slave scheme. To use this scheme, exchange volumes are created in both inputs and act as interface between both domains as depicted in Figure 5. Through these volumes, as shown in Figure 6, the Master sends variables to the Slave at the beginning of the time step, then the Slave advances of time step, from T^n to T^{n+1}. After

Hector Lopez, Alessandro Petruzzi, Walter Giannotti, Domenico De Luca, MELCOR-To-MELCOR Coupling Method in Severe Accident Analysis Involving Core and Spent Fuel Pool, Journal of Energy, vol. 71 Number 2 (2022), 23–28
https://doi.org/10.37798/2022712421

advancing, the Slave sends variables back to the Master following the equation (1).

$$X = aX^{n} + bX^{n+1} \quad (1)$$

Where:

X is the variable exchanged;

"a" and "b" are constants and equal to 0.5 (Crank-Nicholson).

After receiving the variables, the Master advances of time step, from T^{n} to T^{n+1}. This process is repeated with the updated values until the convergence check is passed. Using this methodology allows for a consistent energy and mass flow rates exchange between the domains that results in pressure calculation carried out independently on each domains. Due to these facts, the semi-implicit methodology results in a more stable and self-correcting coupling scheme and in consequence, it is used for the development of a coupling methodology.

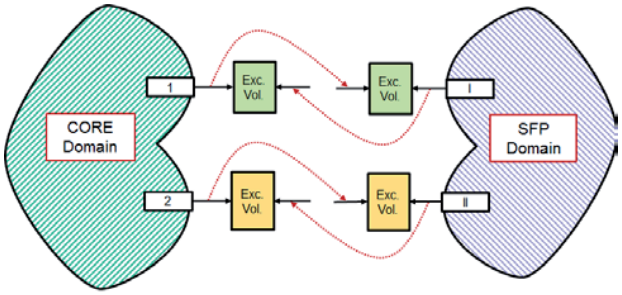

Fig. 5: Schematic of Semi-Implicit Coupling Methodology.

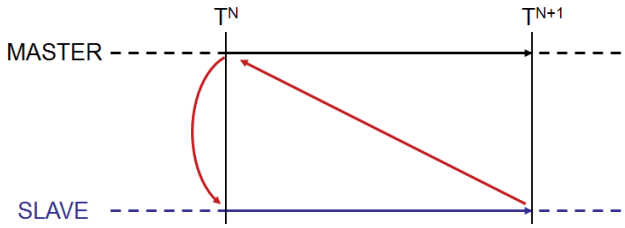

Fig. 6: Semi-Implicit Coupling Methodology Time Step Advancement.

After selecting a semi-implicit approach, a coupling method has been developed at N.IN.E. for MELCOR 1.8.6. In order to create this new methodology, a dedicated Python coupling supervising script has been designed with the purpose of managing the MELCOR-to-MELCOR data exchange. MELCOR 1.8.6 has been selected initially because its numerical card identification and syntax and are easier to implement in the Python script than the alphanumeric approach used in newer versions of the code.

The Python script design is based on the generation and update of restart data at each time step. As depicted in Figure 2, after the generation of the restart file at a given time step, T^{n}, the data required is extracted from the output and sent to the corresponding input through dedicated control functions. At the same time, the size of the restart file is restrained by the use of MELCOR options in the EXEC package to avoid large size files. At each time step, after receiving the corresponding data through the control functions, a new input file for each domain is generated with the updated CF values. Once the semi-implicit convergence check is met, the code advances the simulations to the next time step, T^{n+1}.

The script includes the possibility to select the coupling exchange variables , "a" and "b" from equation (1). In addition, a time step handler is also implemented in case that the convergence is not reached. This design allows for a synchronous coupling (data exchange on every time step) meaning that the coupling time step is equal to the calculation time step at any given moment.

As a semi-implicit methodology, the Python scrip requires the presence of interface elements between the domains to allow the data exchange. The script is designed for two different types of interface elements; exchange volumes and exchange heat structures.

- Exchange volumes are used for material and enthalpy exchange between the two domains. The energy and mass flow rates are exchanged through the coupling algorithm while the pressure is computed independently at exchange volume and used to perform the convergence check;
- Exchange heat structures for heat exchange between the two domains. The boundary temperatures are exchanged through the coupling algorithm while the heat flux is computed independently at the exchange heat structure and used to perform the converge check.

Fig. 7 depicts the exchange elements between the CORE and SFP domains in a VVER-1200.

At this stage of development, the information exchange related to the RN package is not considered, but it will be implemented in later stages.

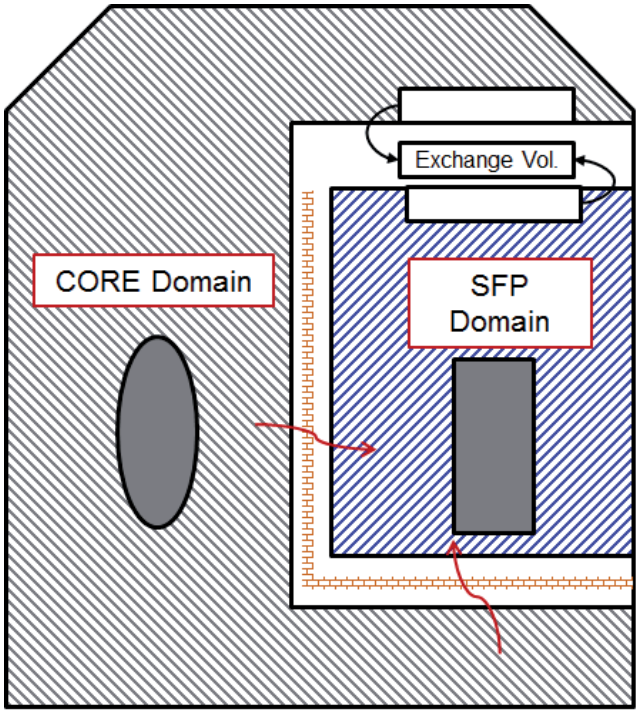

Fig. 7: VVER-1200 Exchange Elements.

III. Proof of Concept Scenario – Description

The main objective of the development of the coupling mechanism is to analyze the effect of the SFP in accidents in VVER-1200 by using a MELCOR-to-MELCOR coupling to circumvent the uniqueness of the COR package and having, effectively, two active cores.

Prior to implement the coupling methodology into a fully scaled VVER-1200, a proof of concept was redeemed necessary to validate the developed Python supervising script. A simplified nodalization, depicted in Figure 8, has been designed to represent both, CORE and SFP domains with the containment dome acting

Hector Lopez, Alessandro Petruzzi, Walter Giannotti, Domenico De Luca, MELCOR-To-MELCOR Coupling Method in Severe Accident Analysis Involving Core and Spent Fuel Pool, Journal of Energy, vol. 71 Number 2 (2022), 23–28
https://doi.org/10.37798/2022712421

as exchange volume. The nodalization uses the operational and geometrical parameters of a prototypical VVER-1200 for the RPV and SFP but with a simplified PS/SS and containment.

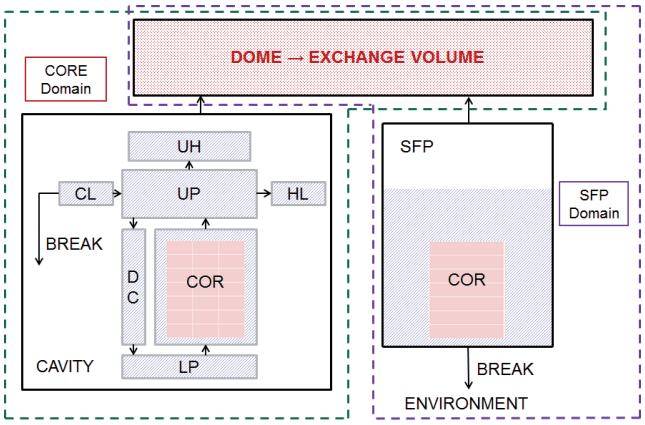

Fig. 8: Proof of Concept Nodalization.

As mentioned above, the nodalization depicted in Figure 8 describes both CORE and SFP domains as follows.

- CORE domain, in green, includes
  - RPV formed by 5 CVs; LP, core, DC, UP and UH filled with water;
  - COR package of 3 rings and 7 axial levels. This COR package reproduces the LP and active core region cells from EL 16.93 m to EL 22.38 m. The first three levels represent the LP internals while levels 4-7 represent the active core;
  - Main loops formed by 2 CVs; HL and CL filled with water;
  - RPV Cavity of 294 m^3;
  - Containment dome of 500 m^3 acting as the exchange volume;
  - Break that connects the CL with the RPV cavity (0.01 m^2, 2% of the CL area).
- SFP domain, in purple, includes
  - SFP of 200 m^3 and 7.4 m water level;
  - COR package of 1 ring and 7 axial levels to reproduce the spent fuel. This COR package reproduces the spent fuel assembly cells from EL 20.7 m to EL 24.8884 m. Level 3-6 represent the fuel region of the spent fuel assembly. Levels 1, 2 and 7 represent the region of the assembly below and above the fuel.;
  - Containment dome of 500 m^3 acting as the exchange volume;
  - The environment;
  - Break that connects the SFP with the environment (0.01 m^2).

Table 1 shows the initial conditions applied to the nodalization as well as the main events of the transient. The core COR package generates a power equal to 3GWt of operating power decay heat while the SFP COR package power has been assumed constant through all the transient.

Initially, all the cells of both COR packages are well submerged in water while both domains are stable on normal operation conditions as shown in Table 1. At the start of the transient, both breaks occur simultaneously at the CL and at bottom of the SFP.

The breaks used in the scenario have been arbitrary sized; the objective is to set up a small break on each location in order to have slower mass depletion and observe the transient clearly

Table 1: Initial Conditions and Main events.

INITIAL CONDITIONS	
Primary Side	
Property	**Value**
Pressure [MPa]	15.7
Temperature [K]/[°C]	570/297
Core power [MW]	3000
Containment	
Pressure [MPa]	0.1
Temperature [K]/[°C]	330/57
SF decay power [MW]	5
Environment	
Pressure [MPa]	0.1
Temperature [K]/[°C]	293/20
MAIN EVENTS	
CL break opening time [s]	0.0
SFP loss of coolant time [s]	0.0

IV. Proof of Concept Scenario — Results

Once the nodalization has been defined, the transient is simulated by running both inputs (one dedicated to each domain) and the Python script. For this scenario, the CORE input has been established as the Master while the SFP has been established as the Slave for the semi-implicit methodology purposes. The transient described in Section 3 is simulated for 1000 s. The objective is to prove that the Python script is able to manage the data exchange providing reliable results while simulating the evolution of two COR packages under different conditions. In the next figures, the main results are discussed.

Figure 9 shows the pressure in all the containment-related CVs; the cavity, the SFP and the containment dome. All three compartments present identical behavior despite being in different inputs (cavity is in the CORE domain while SFP is in the SFP domain and the containment dome is in both of them) implying that the script is able to keep the convergence of the pressure at each time step of the transient.

The pressure suffers an initial increment until the water inventory of the primary system is released into the cavity at which point starts to stabilize until the complete depletion of the SFP at around 280 s due to the release of SFP water into the environment. At this point, the containment suffers a depressurization.

The situation originated in the primary system due to the break in the CL at 0.0 s causes a sudden depressurization of the system and a massive relocation of the RPV water into the cavity compartment. Figure 10 shows how the core is completely uncovered in 60 s after the break. On the other hand, the SFP suffers a slower depletion due to the mass relocation into the environment and its COR package is not fully uncovered until 280 s.

Hector Lopez, Alessandro Petruzzi, Walter Giannotti, Domenico De Luca, MELCOR-To-MELCOR Coupling Method in Severe Accident Analysis Involving Core and Spent Fuel Pool, Journal of Energy, vol. 71 Number 2 (2022), 23–28
https://doi.org/10.37798/2022712421

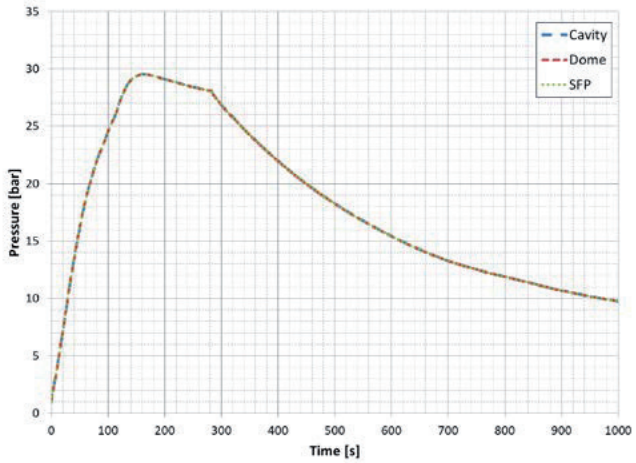

Fig. 9. Containment Pressure.

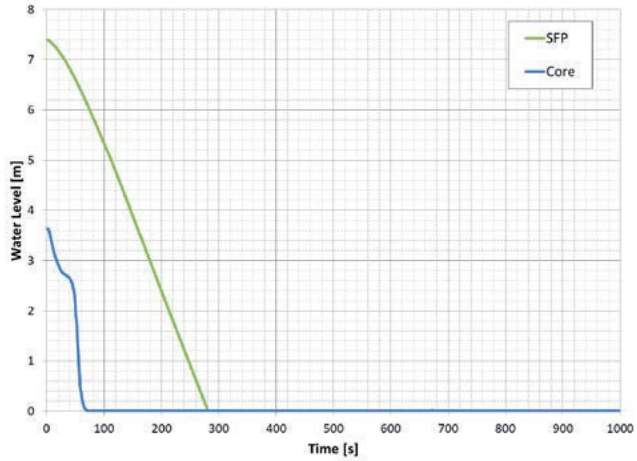

Fig. 10. Core Region and SFP Water Level.

Besides the convergence of the pressure between both domains, the most important parameters to evaluate are those related to the COR package. Figure 11 and Figure 12 depict the cladding temperatures of the CORE domain COR package (channel 1) and the SFP domain COR package respectively. The temperatures depicted correspond to the axial levels with active fuel (4-7 for CORE and 3-7 for SFP).

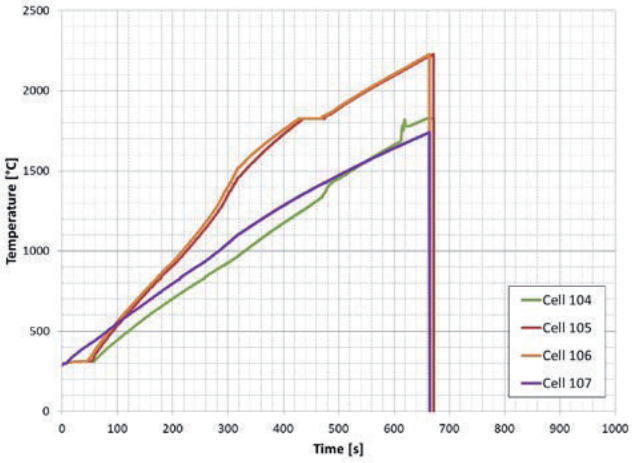

Fig. 11. CORE Domain Cladding Temperature.

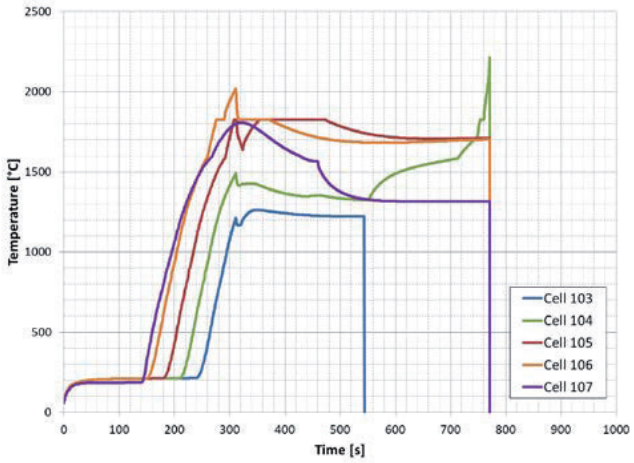

Fig. 12. SFP Domain Cladding Temperature.

As expected, despite being connected, each COR package predicted a different evolution based on the transient conditions.

First, the CORE domain temperatures started to increase right after the core became uncovered at 50 s due to the decay heat of the fuel. The temperature kept rising on an steady paste due the lack of any recovery mechanism with the oxidation and H2 release once the temperature surpass the 1100 °C at around 220 s (Figure 15). The code predicted a complete collapse of the channel 1 of the core around 650 s after the break. This relocation into the LP caused the eventual failure of the lower head.

The temperatures of the SPF, on the other hand, are kept under control until the COR cells start to be uncovered. In this case, the onset of the temperature rise for each cell is clearly differentiated since the SFP level decreases much more slowly that in the RPV (Figure 10). Finally, the code predicts a complete collapse around 780 s.

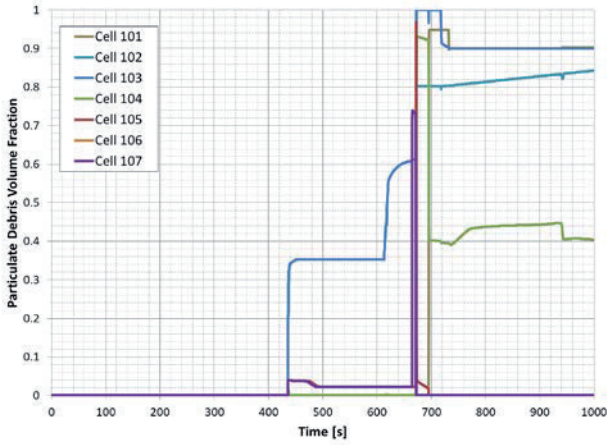

Fig. 13. CORE Domain Particulate Debris Volume Fraction

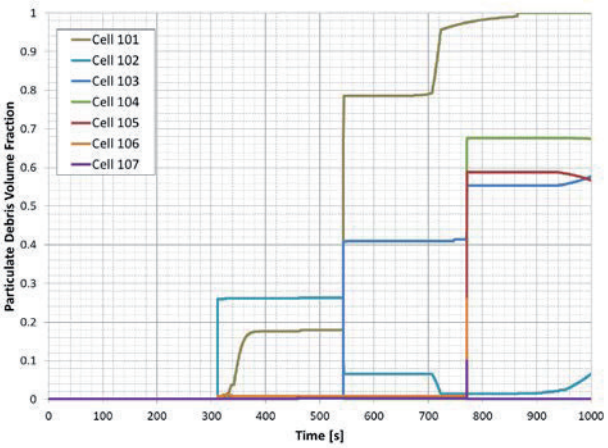

Fig. 14. SFP Domain Particulate Debris Volume Fraction.

Hector Lopez, Alessandro Petruzzi, Walter Giannotti, Domenico De Luca, MELCOR-To-MELCOR Coupling Method in Severe Accident Analysis Involving Core and Spent Fuel Pool, Journal of Energy, vol. 71 Number 2 (2022), 23–28
https://doi.org/10.37798/2022712421

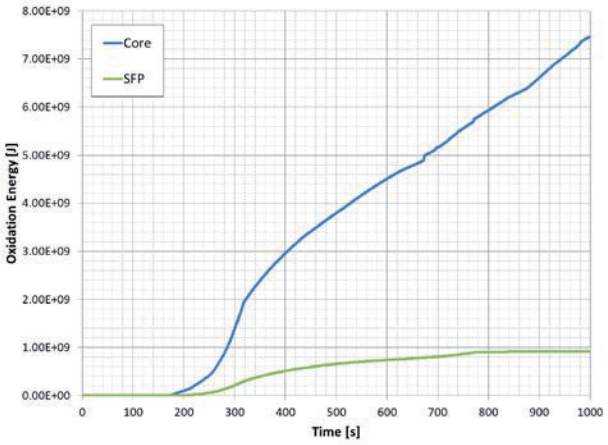

Fig. 15. Oxidation Energy.

Analogously to the cladding temperatures depicted in previous figures, Figure 13, Figure 14 and Figure 15 present other COR-related parameters; the particulate debris and the oxidation energy. Analogously to the cladding temperatures, each domain presented an independent core degradation.

Lastly, it is worth saying that the additional time added by the coupling into the simulation time has been negligible but this is mainly due to the simplicity of the simulation model used for the proof of concept. Further analysis on full NPP simulation models have to be performed in order to address the real impact on the simulation time.

The results presented in this Section, although being from a simple proof of concept, are encouraging results as they demonstrate that the coupling mechanism developed at N.IN.E. is capable to capture both core degradation independently while continuously manage and supervise the data exchange so any phenomena occurring in one domain can affect the other.

V. Future Work

With the final goal in mind, the next step will be the implementation of the interface heat structures to validate if the heat transfer and boundary temperatures between the domains are correctly predicted. Once that is validated, the implementation of the coupling mechanism into a fully scaled VVER NPP, as the one depicted in Figure 16 and Figure 17, will be performed.

With the final implementation, the analysis of selected scenarios involving the RPV and the SFP will be performed.

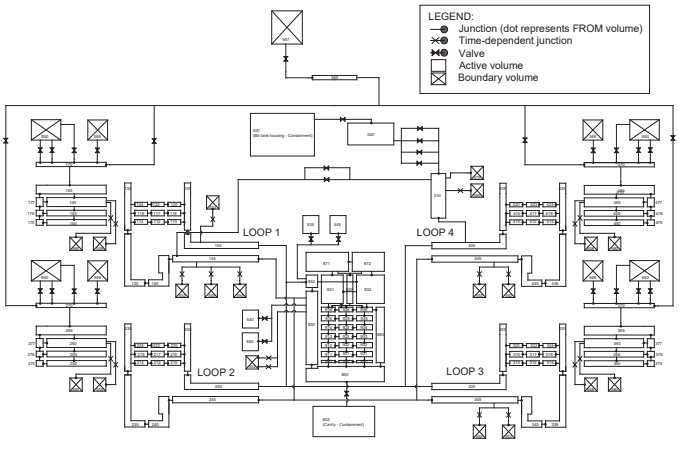

Fig. 16: VVER NPP Primary/Secondary System Nodalization.

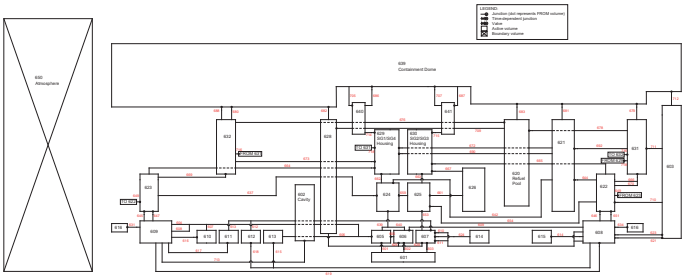

Fig. 17. VVER NPP Containment Nodalization.

VI. Conclusions

As stated at the beginning of the paper, the RPV is not the only source of fission products in the containment as the SFP hosting the depleted fuel is, in some NPP, inside the containment and SA conditions can occurs in the pool. The impact of the SFP H2 directly released into the containment can alter the expected evolution of a given transient. This becomes even more relevant in reactors having proximity between the RPV and SFP such as the VVER-1200. This close proximity implies that any SA occurring in the SFP potentially affects the RPV and vice-versa.

As such, the main objective of the present paper was to establish a coupling mechanism for MELCOR that allowed to circumvent the code limitation of one unique COR package in order to analyze accidents that may involve both, the RPV and the SFP. One of the requirements was that this mechanism should be used even if access to the source code was not possible. This was performed by N.IN.E. by developing a coupling mechanism using a dedicated Python supervising script. This scrip manages the data exchange between the different domains (inputs) by a semi-implicit scheme and updates the corresponding input at each time step with dedicated control functions.

The results from the proof of concept presented in this paper proved to be encouraging that demonstrated the capabilities of the aforementioned coupling, being able to capture both core degradation independently while continuously managing the data exchange. In addition, the tax observed on the simulation time due to the coupling was negligible most certainty due to the simplicity of the simulation model used. Although further analysis are required in more complex nodalization in order to assess the real impact.

The future steps involve further validation of the capabilities of the mechanism in order to perform its final implementation in a real VVER reactor nodalization and the analysis of the subsequent accident scenarios involving the SFP as a secondary core.

References

[1] NRC, "*MELCOR Computer Code Manuals Vol. 1: Primer and Users' Guide Version 1.8.6*", NURE/CR-6119, Vol.1, Rev. 3, SAND 2005-5713, Washington, September 2005.

[2] NRC, "*MELCOR Computer Code Manuals Vol. 2: Reference Manuals Version 1.8.6*", NURE/CR-6119, Vol.2, Rev. 3, SAND 2005-5713, Washington, September 2005.

[3] R. K. Cole, Jr. "*Coupling of MELCOR to Other Codes under an Executive Program using PVM Message Exchange*", 2002 RELAP5 Users Seminar, Park City, Idaho, September 4-6 2002.

[4] W. L. Weaver, E. T. Tomlinson, and D. L. Aumiller, "*An Executive Program for use with RELAP5-3D©*," B-T-3394, 2001 RELAP5 Users Seminar, Sun Valley, Idaho, September 5-8 2001.

[5] Aumiller, D. L., Tomlinson, E. T., Bauer, R. C., 2001a, "*A Coupled RELAP5-3D/CFD Methodology with Proof-of-Principle Calculation*" Nuclear Engineering and Design, Vol. 205, pp 83-90.

Hector Lopez, Alessandro Petruzzi, Walter Giannotti, Domenico De Luca, MELCOR-To-MELCOR Coupling Method in Severe Accident Analysis Involving Core and Spent Fuel Pool, Journal of Energy, vol. 71 Number 2 (2022), 23–28
https://doi.org/10.37798/2022712421

Journal of Energy
VOLUME 71 Number 2 | 2022
journal homepage: http://journalofenergy.com/

Power Variability of Wind and Solar Production Portfolio in the Republic of Croatia (March 2023)

Laszlo Horváth, Danijel Beljan, Miroslav Elezović, Andrea Marić

***Summary* — In this work, we analysed multi-annual data set of wind and solar production portfolio with different power frequency approaches and averaging methods in order to characterize power production variability at different temporal scales. All the methods have their advantages depending on their scale and purpose, but also some shortcomings that limit their use. For the purposes of this work, we selected the method of explicit derivation as the most appropriate for the fast power change frequency analysis and characterization. The variability of power production from wind and solar power plants in Croatia is strongly present on an hourly, daily and seasonal level, while on an annual level the variability is much less pronounced. Since current electricity production and consumption must remain in balance to maintain the stability of the power network, this variability of production can pose significant challenges for the inclusion of large amounts of wind and solar energy in the power system of the Republic of Croatia. A particular challenge for the power system in terms of production variability is the fast change in power. Fast power change affects the quality of production forecasting and consequently causes higher imbalance costs. The impact on the management and balancing of the power system is particularly challenging.**

***Keywords* — fast power change, solar power plants, variability of electricity production, wind power plants**

I. Introduction

CROATIAN ENERGY MARKET OPERATOR Ltd. (HROTE) in accordance with the Law on the Renewable Energy Sources and High-Efficiency Cogeneration ("Official Gazette", number: 138/21) is designated as the manager of the ECO balance group with the obligation to forecast the production of ECO balance group, payment of balancing costs for ECO balance group and sale of electricity from ECO balance group.

The installed capacity of wind power plants (WPP) in the Republic of Croatia is growing rapidly, on 31 December 2021 it was 989.5 MW, while in the ECO balance group there was 712 MW of installed power of WPP on the same day. Considering that the largest share of the installed power of WPP in the Republic of Croatia is in the ECO balance group, for the purposes of this paper, data of production of WPP (the same applies to solar power plants) from the ECO balance group will be used as representative for the Republic of Croatia.

The construction of solar power plants (SPP) in the Republic of Croatia is currently lagging behind WPP, but significant increase in the installed power of SPP is expected in the next few years. On 31 December 2021, the installed capacity of SPP that are part of the ECO balance group was 55.9 MW.

The variability of electricity production from WPP and SPP is expressed on an hourly, daily and seasonal level, while on an annual level the variability is less pronounced [1]. A particular challenge for the power system in terms of production variability is the fast change in power. Fast power change affects the quality of production forecasting and consequently causes higher imbalance costs, and the impact on the management and balancing of the power system is particularly pronounced [2], [3].

Considering the biggest share of the installed power of WPP in total power of all plants that are part of ECO balance group, the quality of WPP production forecasting has the greatest impact on the balancing costs for the ECO balance group. In 2021, HRK 53.56 million of balancing costs were charged to ECO balance group, and according to HROTE's estimation, WPP used more than 97% of all the costs. The achieved quality of WPP forecast for a day ahead in 2021 was 4.92% MAE (35.5 MWh/h) with a maximum positive error (production greater than plan) of +268 MWh/h and with a maximum negative error (production less than plan) of -221 MWh/h. With forecasting WPP production on the day of delivery, the total WPP forecasting error was reduced for 25%, from an average of 35.6 MWh/h to 26.7 MWh/h, that is, from MAE 4.92% to MAE 3.70%. The paper will specifically analyse the quality of the WPP forecast, in case of fast power change, for a day ahead and on the day of delivery.

The achieved quality of SPP production forecast for a day ahead in 2021 was 1.73% MAE (<1 MWh/h) with a maximum positive error of 10 MWh/h and with a maximum negative error of -16 MWh/h.

The paper presents an analysis of the frequency of fast power change, WPP and SPP ramp events, individually and in total, which are part of the ECO balance group, the amount and distribution of fast power change in time. The impact of fast power change on the entire power system will also be considered and analysed in paper. For the purposes of the analysis, historical 15-minute, hourly and 2-hour data of WPP and SPP production were used for the first

(Corresponding author: Laszlo Horvath)
Laszlo Horvath, Danijel Beljan, Andrea Marić and Miroslav Elezović are with the Croatian energy market operator (HROTE)
Zagreb, Croatia (e-mails: laszlo.horvath@hrote.hr, danijel.beljan@hrote.hr, andrea.maric@hrote.hr, miroslav.elezovic@hrote.hr)

Laszlo Horváth, Danijel Beljan, Miroslav Elezović, Andrea Marić, Power Variability of Wind and Solar Production Portfolio in the Republic of Croatia (March 2023), Journal of Energy, vol. 71 Number 2 (2022), 29–34
https://doi.org/10.37798/2022712408

three years and four months of ECO balance group operation, and additionally, an analysis was made for a shorter period based on minute data of WPP production.

II. Literature Overview

Wind and solar power production variability, identification of fast power change events and how they affect the quality of production forecasting and power system management was widely studied subject due to strong impact on the grid integration, flexibility requirements and accuracy of wind and solar power forecasts.

In research article [4] a wind energy Ramp Tool and Metric (RT&M) was developed with description of multiple methods how to identify events of fast power change. The RT&M integrates skill of multiple forecast models over a matrix of ramp events of varying amplitudes and durations, with range of power thresholds and window lengths.

Report [5] presents an overview of current fast power change (ramp) definitions and state-of-the-art approaches in ramp event forecasting. Multiple ramp definitions are quoted in report and ramp forecasting models are described.

In paper [6] an analysis of time series of load, wind, PV and the resulting net load is presented in scenarios for Europe that allow to quantify flexibility requirements in future power systems with high shares of variable generation in scenarios for Europe that allow to quantify flexibility requirements in future power systems with high shares of variable generation. Ramp properties of wind and PV generation in Europe are described with comparison of expected range of largest wind and solar power ramps on hourly level.

Article [12] and study [13] are focused on assessment of the possibility of the integration of wind power plants specifically into the electric power system of the Republic of Croatia. Since wind power variations affects power system requirements in ancillary services, an assessment of fluctuation in the power output of wind power plants is made. Based on model data an assumption is made of maximum hourly fluctuation on entire expected wind portfolio in the Republic of Croatia.

III. Description of the Method and Input Data

According to [4], the analysis of the frequency of events of fast power change of WPP and SPP, individually and collectively, can be performed according to three described methods:

A. → Fixed-time interval method – the method with constant time intervals

The method with constant time intervals records the change in power between the initial and final power values of a given time interval, which can be bigger or smaller than the given power change value. Due to the simplicity of implementation, the method itself has several disadvantages, such as the occurrence of larger power changes within the observed interval and overlapping positive and negative power changes, where only a change in one direction, either positive or negative, is recorded. In the case when we analyse 15-minute power data of WPP in a time period of 2 hours, the comparison will be made only of the first and last 15-minute intervals. Within the analysed interval there may be larger power changes, but they will not be considered.

B. → Minimum - maximum method - the method of the lowest and highest value

Considering the shortcomings of the previous method, the lowest and highest value method identifies the lowest and highest value in each time interval and thus identifies the most cases with fast power change. In the case when we analyse 15-minute power data of WPP in a time period of 2 hours, we will compare each 15-minute interval and look for the lowest and highest value of all 15-minute intervals in the 2-hour time period.

C. → Explicit derivation method

The method compares each interval with the adjacent interval of a given time period and looks for a power change that is above the given power change value. The method analyses all power values within a given time interval. In the case when we analyse 15-minute power data of WPP in a time period of 2 hours, each 15-minute interval is compared with the next 15-minute interval, and if the power change is greater than the set value, it is recorded as a fast power change event.

Although a fast power change can be easily identified visually, there is no consensus on the accepted formal definition of a fast power change, and it can be characterized according to three features: direction, magnitude and duration [5], [6], [7], [8].

The highest rates of change in WPP power depend on the geographical size of the observed country. In medium-sized and large countries, the maximum hourly change in the WPP power is in the range of 6-10% of the installed WPP capacity, while in smaller countries it is in the range of 11-18%. SPP have a power change equal to or close to 0 for almost half of the hours because they have no production during the night hours, and in most countries the maximum power change at the hourly level is in the range of 18-25% of the installed capacity [9].

For the purposes of this work, the method of explicit derivation was used, with the fact that the distribution of all changes in power will be shown without clearly determining the threshold that would determine the fast power change for the observed time period.

The input data for calculating the power change of WPP and SPP are historical 15-minute data on the production of WPP and SPP for the period from January 1, 2019 to May 1, 2022, from which hourly and two-hourly historical data were obtained. For a shorter time period from March 2, 2022 to June 17, 2022, an analysis of the power change of the WPP was made for one-minute and 5-minute intervals.

IV. Results and Interpretation

As stated in the previous chapter, the paper will analyse the power change based on the method of explicit derivation according to which the power change is equal to the difference between the power in interval i and the power in the previous i-1 interval in relation to the total installed capacity (1).

$$\Delta P_i = \frac{P_i - P_{i-1}}{P_{inst}} \quad (1)$$

Additionally in chapter 4.B. for the hourly time interval for WPP, a threshold for fast power change was determined (10% of the installed capacity of the WPP), and the quality of forecasting was determined for such a determined fast power change.

A. → Analysis of WPP and SPP power change distribution

Figures 1-3 show the distribution of all changes in WPP power at the 2-hour, hourly and 15-minute levels.

Laszlo Horváth, Danijel Beljan, Miroslav Elezović, Andrea Marić, Power Variability of Wind and Solar Production Portfolio in the Republic of Croatia (March 2023), Journal of Energy, vol. 71 Number 2 (2022), 29–34
https://doi.org/10.37798/2022712408

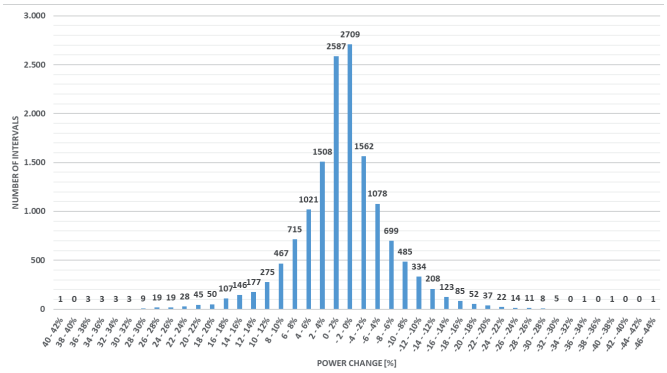

Fig. 1. Distribution of the WPP power change intervals at the 2-hour level

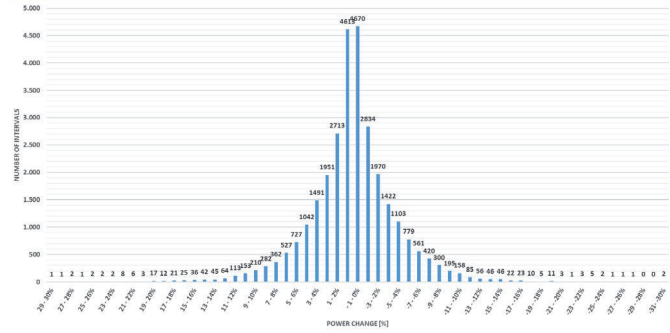

Fig. 2. Distribution of the WPP power change intervals at the hourly level

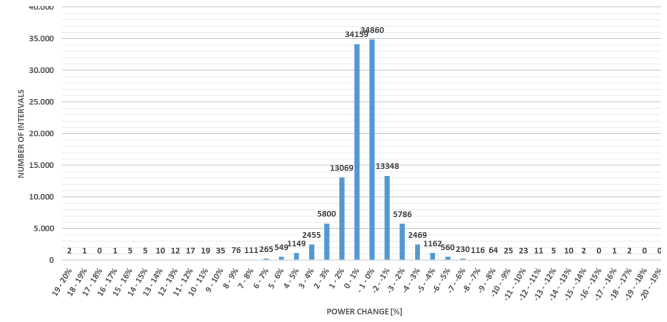

Fig. 3. Distribution of the WPP power change intervals at the 15-minute level

At the 2-hour interval, the largest power increase was recorded in the amount of +40.2% of the installed capacity, and the largest decrease was -45.4%. At the hourly interval, the previously described range is +29.7% and -30.8%, and at the 15-minute level +19.6 and -17.5%. If we compare the results of the research under [9], according to which in smaller countries the maximum WPP power change on an hourly level is in the range of 11-18%, we can conclude that significantly larger power changes occur in the Republic of Croatia than the average. The characteristics of the wind and the concentration of WPP in a relatively small area are the main cause for extremely fast WPP power changes in the Republic of Croatia.

Figure 4 shows the normal distribution of WPP power changes at 2-hour, hourly and 15-minute levels.

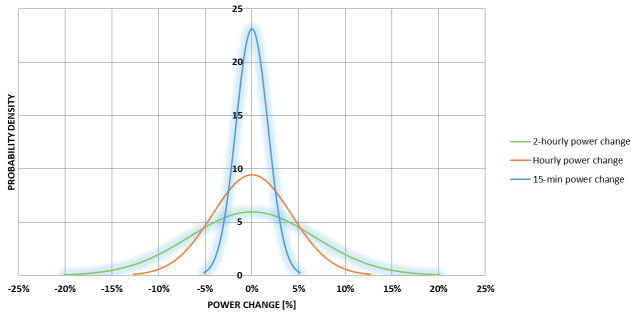

Fig. 4. Comparative presentation of the normal distribution of the WPP power change at the 2-hour, hourly and 15-minute levels

The data in Figure 4 for each time period are in the range 0% +/- 3% standard deviation of all data and include 98.4% of all data, so for a 2-hour period they are in the range +/-20.1%, for an hour period in the range +/-12.7%, and for a 15-min period in the range +/-5.2% of the installed WPP capacity.

Figures 5 and 6 show the distribution of WPP power changes at the minute and 5-minute levels for the period from March 2, 2022 to June 17, 2022.

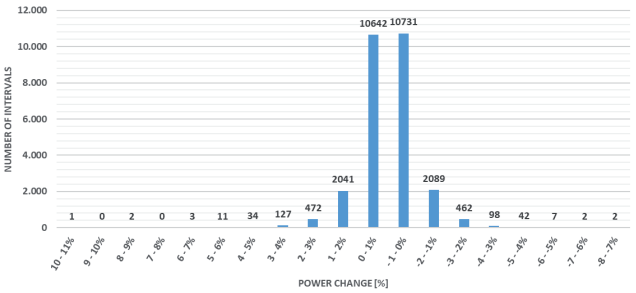

Fig. 5. Distribution of the WPP power change intervals at the 5-minute level

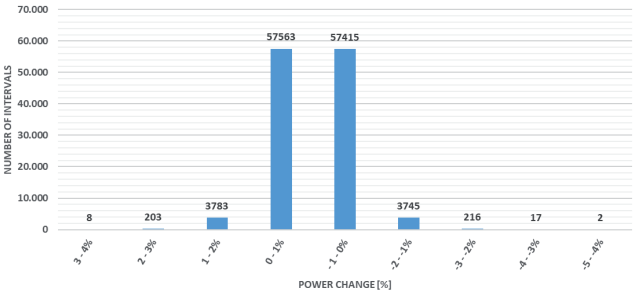

Fig. 6. Distribution of the WPP power change intervals at the 1-minute level

The largest change in WPP power at the 5-minute level is +10.3% and -7.2%, while at the 1-minute level it is in the range of +3.6% and -4.6% of the installed WPP capacity.

Figure 7 shows the distribution of the change in WPP power at the hourly level of more than 10% of the installed WPP capacity within a day.

Laszlo Horváth, Danijel Beljan, Miroslav Elezović, Andrea Marić, Power Variability of Wind and Solar Production Portfolio in the Republic of Croatia (March 2023), Journal of Energy, vol. 71 Number 2 (2022), 29–34
https://doi.org/10.37798/2022712408

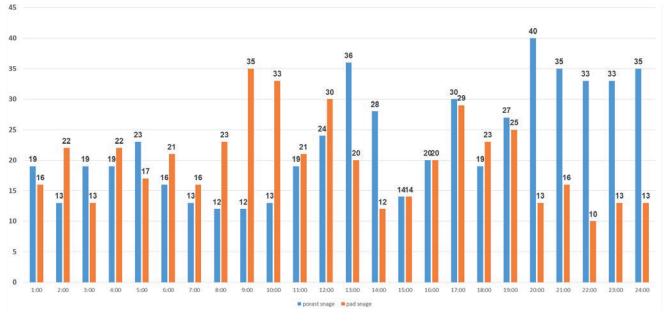

Fig. 7. Distribution of fast WPP power change intervals within a day

It can be seen from Figure 7 that the fast increase in WPP power on an hourly basis is most common towards the end of the day (20:00 to 24:00), while the fast decrease in WPP power is most common in the morning hours (9:00 to 10:00). No analysis was performed for other time levels and thresholds of power increase, but the authors assume that similar results would be obtained. Similar results are shown in paper [10] where fast wind power change in California, USA is analised.

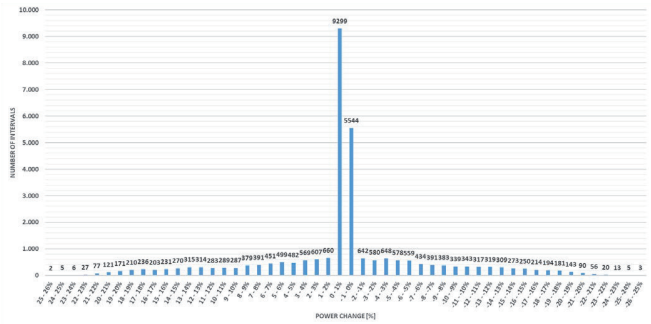

Fig. 8. Distribution of SPP power change intervals at hourly level

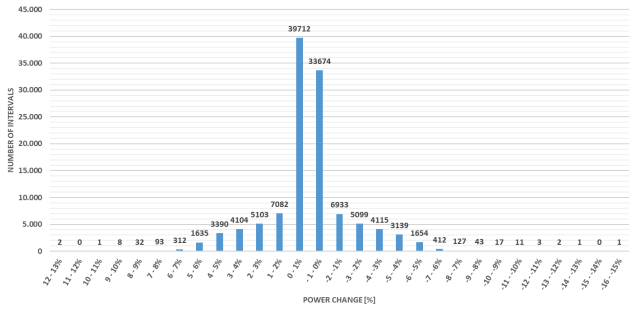

Fig. 9. Distribution of SPP power change intervals at 15-minute level

Figures 8 and 9 show the distribution of all SPP power changes at hourly and 15-minute levels. The largest change in SPP power at the hourly level is +25.1% and -25.9%, while at the 15-minute level it is in the range of +12.3% and -15.6%, of the installed SPP capacity. Compared to the research results under [9], according to which the maximum power change on an hourly level is in the range of 18-25% of the installed capacity, it follows that the maximum power change of SPP in the Republic of Croatia is at the upper limit of the specified range. The paper additionally analysed the distribution of the power change for a hypothetical case according to which the installed SPP capacity in the previous period would have been 13 times higher (increase from 54 to 698 MW), which would have made the installed SPP capacity roughly equal to the WPP capacity. Increased SPP capacity was made in simplified way where existing historical dana was linearly increased in all hours.

Figures 10 and 11 show the distribution of all power changes for the previously described hypothetical case at hourly and 15-minute levels.

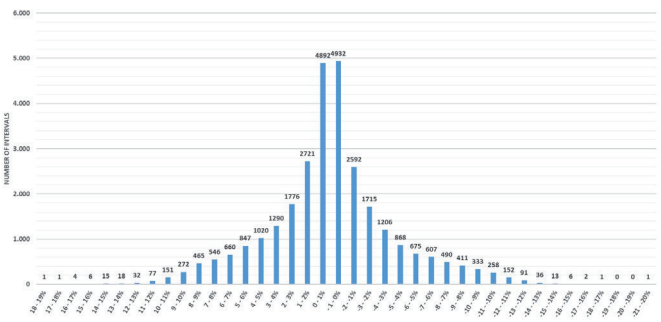

Fig. 10. Distribution of the power change intervals for the hypothetical case of a combination of WPP and SPP at the hourly level

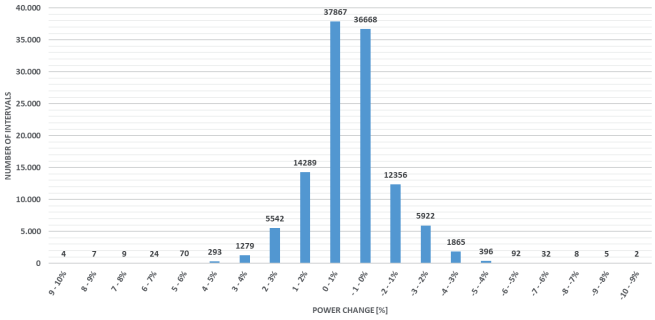

Fig. 11. Distribution of the power change intervals for the hypothetical case of a combination of WPP and SPP at the 15-minute level

The largest change in SPP and WPP power for the specified hypothetical case at the hourly level is +18.0% and -20.9%, while at the 15-minute level it is in the range of +9.8% and -9.0% of the installed SPP and WPP capacity.

B. → WPP forecasts under conditions of fast power change

From January 1, 2019, HROTE plans the production of WPP on the day of delivery in a way that it corrects the WPP production plan made on the previous day for the day of delivery several times a day (hourly). The correction of the WPP forecast is coordinated with the allocation of cross-border transmission capacities, so it is done at least one hour before the delivery hour.

In this chapter, we will analyse the quality of WPP forecasts for a day ahead and on the day of delivery (intraday) in the case of fast WPP power change on an hourly basis. For the purposes of the following analysis, any change greater than 10% of the installed capacity of all WPP will be considered as a fast power change. Table I shows the quality of the WPP production forecast with fast power changes on an hourly basis in the period from January 1, 2019 to May 1, 2022.

TABLE I
WPP FOORECAST QUALITY IN CASE OF POWER CHANGE

Change in WPP power	Number of intervals	WPP day-ahead forecast quality MAE [%]	WPP intraday forecast quality MAE [%]	Difference [%]
>0%	14458	5.06%	4.17%	-17.56%
>10% <15%	413	9.12%	8.34%	-8.63%
>15% <20%	111	12.21%	11.48%	-5.97%
>20%	28	14.36%	14.96%	**4.21%**
<0%	14719	4.85%	4.05%	-16.46%
>-10% <-15%	387	7.77%	7.25%	-6.69%
>-15% <-20%	71	9.86%	9.40%	-4.62%
>-20%	19	11.48%	12.65%	**10.25%**

With the increase in power at the hourly level, HROTE achieved a total forecast quality of 5.06% MAE (Mean Absolute Error) for the day ahead, while in the intraday the forecast error was re-

Laszlo Horváth, Danijel Beljan, Miroslav Elezović, Andrea Marić, Power Variability of Wind and Solar Production Portfolio in the Republic of Croatia (March 2023), Journal of Energy, vol. 71 Number 2 (2022), 29–34
https://doi.org/10.37798/2022712408

duced by 17.56%, to 4.17% MAE. In the hourly power drop on the day of delivery, the error was reduced by 16.46%, from 4.85% to 4.05% MAE. With fast power changes (>10% of the installed capacity), significantly worse forecast quality was achieved, and an additional drop in forecast quality was noticeable with faster power changes. With faster power changes, a drop in the quality of forecast corrections on the day of delivery is also noticeable. In contrast to all hours, where the total forecast was improved by 16.46% and 17.56%, significantly lower levels of forecast quality improvement were achieved with fast power changes. With extreme power changes, even worse quality of the WPP forecast was achieved in the intraday than was a day ahead. The reason for the worsening of the forecast in the intraday is that on the day of delivery the forecast is planned at least an hour in advance, which in the conditions of unstable weather resulting in fast power change can be considered a relatively long period for replanning WPP production. If it were possible to plan closer to the delivery time and for shorter balancing periods, it would be possible to improve the quality of the WPP forecast in case of fast power change [11].

V. Application Of Results

This paper presents empirical data on the variability of WPP and SPP production at different time intervals, using the method of explicit derivation. Since the installed power of SPP is significantly smaller than the installed power of WPP in the Republic of Croatia, a hybrid system of WPP + SPP with equal shares was hypothetically set up based on real data. The goal of the mentioned hybrid system is to enable the analysis of the impact of the technological portfolio on the production of electrical energy, i.e. the hybridization of production.

Although many studies on the possibility of integrating variable sources into the Croatian electric power system (EPS) have been made, they are, as a rule, based on model data of WPP (and SPP) operation. This work aims to contribute to the understanding of the characteristics of the operation of WPP and SPP, primarily their real variability based on the operation data of the power plants included in the ECO balance group. That would lead to facilitation of similar future analyses and enabling easier planning of the necessary measures and interventions in the system, with the aim of greater integration of RES in the Republic of Croatia.

VI. Conclusion

The analysis of the actual variations of production from the ECO balance group WPPs (on a representative sample of 712 MW, during about 3.5 years of analysed data), showed that the model assumptions that were used for the analysis of the necessary interventions in the EPS were adequate and well evaluated. By the same token, these assumptions were somewhat conservative since the frequency of real power changes is somewhat lower than the modelled ones. Necessary interventions in the EPS were required due to the greater integration of variable energy sources (please refer to reference: [12], [13]).

The WPP and SPP operation performance shows the following characteristics of technology specific and whole portfolio power variability:

– expected hourly change of WPP power within the interval from -31% to +30% of installed WPP capacity, whereby 99% of hourly variations of WPP power are within the range of -13.8% to +14.8% of installed WPP capacity, while changes greater than ± 10% of the installed capacity (fast changes in WPP power) can be expected in 3.5% of cases;

– expected hourly change of SPP power is within the interval from -26% to +26% of installed SPP capacity, with 99% of hourly variations of SPP power being within the interval of -20.4% to +20.7% of installed SPP capacity;

– the expected hourly change of a hypothetical hybrid system with similar shares of WPP + SPP is smaller, whereby 99% of the hourly power variations of such a system are within the interval from -12% to +11% of the installed WPP + SPP capacity.

Hourly variations of less than ±10% of installed capacity should not be a problem from the production planning and system balancing point of view. However, hourly changes greater than ±10% of the installed capacity (although relatively rare) represent a special challenge. From the point of view of the production forecast, the error in the case of fast and intense power changes of more than ±10% is significantly higher and reaches about 15%. As the room for forecast improvement in small and moderate power changes is limited (the day-ahead error is about 5%, while the forecast error for the day of delivery is close to 4%), future efforts in forecast improvement should be directed precisely in the direction of reducing the error in fast and intense change in power, both in terms of their intensity and in terms of the moment of their appearance. In addition, it was shown that production planning, except in the case of extreme (and very rare) power changes, results in smaller production forecast errors. Therefore, planning closer to the actual delivery time and for shorter balancing periods, would lead to additional benefits for the system operator, who could plan the necessary engagements of the available regulatory measures with greater reliability.

The presented frequency of hourly power variations in case of system hybridization with an equal amount of WPP and SPP, suggests that for some future portfolio (i.e. 3000 MW of WPP and SPP by 2030), 99% of hourly production variations would be within the interval from -360 MW to +330 MW. When looking at 15-minute power variations, empirical data shows that:

— the expected 15-min power change of the WPP is smaller than the expected hourly power change and ranges from -17% to +20% of the installed WPP capacity, with 99% of the 15-min variation of the WPP power within the range of -5.7% to +5.9% of installed WPP capacity, while changes greater than ±10% of installed capacity (fast 15-min changes of WPP power) can be expected in 0.11% of cases;

— the expected 15-min change in SPP power is smaller than the expected hourly power change and ranges from -16% to +13% of the installed SPP capacity, with 99% of the 15-min SPP power variation within the range from -6.1% to +5.8% of installed SPP capacity while changes greater than ±10% of installed capacity (fast 15-min changes of power SPP) can be expected in 0.018% of cases;

— the expected 15-min change of a hypothetical hybrid system with similar proportions of WPP + SPP is within the range of -10% to +10% of the installed WPP + SPP capacity, with 99% of the 15-min power variation of such a system within the interval of -3.9 % to +3.8% of installed WPP + SPP capacity.

As can be seen, in 99% of cases at the 15-min level (at which the required secondary regulation in the system is usually estimated), the production variability is significantly lower than the hourly one, especially in the case of hybridization of WPP and SPP production. However, still in extreme cases the variations can be very large. Therefore, such variations are very rare, and it is justified to think about the introduction of a production limitation measure for WPP and SPP in cases of threatened EPS security.

Additionally, WPP variability on 1-minute and 5-minute time interval. The use of high-frequency data provides a deeper understanding of WPP natural variability and performance [14]. High-frequency data is also needed for minute-scale forecasting of WPP

that have application in wind turbine and wind farm control, power grid balancing and energy trading and ancillary services [15].

Finally, it should be noted – although it is not explicitly shown in this paper – that the spatial (geographical) diversification of WPP and SPP, including the construction of production facilities on in the continental part of the Republic of Croatia, has favorable effects on the variability of the entire portfolio of power plants. Since that geographical expansion would lead to different regimes of wind and solar radiation, there would be less simultaneity of production. Therefore, in planning the further development of variable sources such as WPP and SPP, this feature should also be considered.

References

[1] C.L. Archer, M.Z. Jacobson, "Geographical and seasonal variability of the global "practical" wind resources", 2013.

[2] D.-A. Ciupăgeanu, G. Lăzăroi, L. Barelli, „Wind energy integration: Variability analysis and power system impact assessment", 2019

[3] X. Yao, B. Yi, Y. Yu, Y. Fan, L. Zhu, „Economic analysis of grid integration of variable solar and wind power with conventional power system", 2020

[4] L. Bianco, I.V. Djalalova, J. M. Wilczak, J. Cline, S. Calvert, E. Konopleva-Akish, C. Finley, J. Freedman, „A Wind Energy Ramp Tool and Metric for Measuring the Skill of Numerical Weather Prediction Models", 2016.

[5] C. Ferreira, J. Gama, L. Matias, A. Botterud, J. Wang, „A Survey on Wind Power Ramp Forecasting", 2010.

[6] A. Bossavy, R. Girard, G. Kariniotakis, "Forecasting Uncertainty Related to Ramps of Wind Power Production", 2012.

[7] A. Florita, B.-M. Hodge, K. Orwig, "Identifying Wind and Solar Ramping Events", 2013.

[8] J. W. Zack, S. Young, J. Nocera , J. Aymami, and Vidal J. "Development and testing of an innovative short-term large wind ramp forecasting system", Proc. European Wind Energy Conf. and Exhibition, Warsaw, Poland, European Wind Energy Association, 2010

[9] M. Hubera, D. Dimkovab, T. Hamacher, „Integration of wind and solar power in Europe: Assessmentof flexibility requirements", 2014.

[10] C. Kamath, "Understanding Wind Ramp Events through Analysis of Historical Data," pp. 1–6 in Proceedings of the IEEE PES Transmission and Distribution Conference and Expo, New Orleans, La., 2010

[11] Greaves, B., J. Collins, J. Parkes, and A. Tindal, "Temporal Forecast Uncertainty for Ramp Events," in Proceedings of the European Wind Energy Conference & Exhibition (EWEC), Marseille, France, 2009

[12] D. Bajs, G. Majstrović, "The feasibility of the integration of wind power plants into the electric power system of the Republic of Croatia", 2008.

[13] D. Bajs, G. Majstrović, S. Knežević, L. Horvath, D. Jakšić, „Analiza potrebnih tehničkih zahvata i aktivnosti u elektroenergetskom sustavu hrvatske s ciljem preuzimanja većeg udjela proizvodnje planiranih VE", study, Energetski institut Hrvoje Požar, 2010.

[14] E. Gonzalez, B. Stephen, D. Ineld, J. J. Melero, „On the use of high-frequency [1] SCADA data for improved wind turbine performance monitoring", J. Phys.: Conf. Ser. 926 012009, 2017.

[15] . Würth, L. Valldecabres, E. Simon, C. Möhrlen, B. Uzunoglu, C. Gilbert, G. Giebel, D. Schlipf, A. Kaifel, „Minute-Scale Forecasting ofWind Power—Results from the CollaborativeWorkshop of IEAWind Task 32 and 36", MDPI, 2019.

ENERGIJA